200 mg of nanoparticles were dispersed in 40 ml solution of 1.0 mg/ml PEI max. The rest of the process was the same as for γ-Fe_2O_3 nanoparticles.

Transfection and preparation of MNP of different densities

HeLa cells from a human cervical carcinoma line were cultured in Dulbecco's modified Eagle medium (DMEM) supplemented with 10 % fetal bovine serum (FBS) and 1 % penicillin–streptomycin (PS). The cells were seeded in 35 mm dishes at a density of 200,000 cells/well on the day prior to transfection. The cells were incubated at 37 °C in a humidified atmosphere containing 5 % CO_2.

To evaluate the dependency of transfection efficiency on the weight of MNPs, solutions of 1 mg/ml PEI max and various densities of PEI max-coated MNPs were prepared. PEI max and PEI max-coated MNPs solutions (7.5 μl) were mixed with 2.5 μg of plasmid DNA expressing enhanced green fluorescent protein (EGFP) in sterile water for 15 min. DNA/PEI max complexes and DNA/PEI max/MNP complexes were added to 1 ml medium. Each medium containing DNA/PEI max complexes or DNA/PEI max/MNP complexes was added to the cells in each sample dish after removing the medium and washing the cells with phosphate-buffered saline (PBS). The weights of PEI max-coated MNPs in each 7.5 μl sample of 1 mg/ml PEI max solution were 0.75, 1.5, 2.25, 3.0, 4.5, and 7.5 μg for both γ-Fe_2O_3 and Fe_3O_4. The amount of plasmid DNA was 2.5 μg for all the samples.

Each dish containing DNA/PEI max/MNP complexes was placed on a neodymium (NdFeB) permanent magnet (diameter = 40 mm, height = 20 mm) purchased from Sangyo Supply Co. for 1 h. Each dish containing DNA/PEI max/MNP complexes was excited using a magnetic field gradient perpendicular to the dish at 26.5–33.0 T/m in the area of the dish near the cell surface. Two days after transfection, its efficiency was evaluated by fluorescence microscopy. The areas of fluorescent cells in fluorescence micrographs were compared with those of all cells observed in phase-contrast micrographs. The ratio of area of the fluorescent cells was calculated. Nine datasets were prepared for each condition of the fluorescence micrographs (three dishes prepared for each condition and three sites observed in each dish).

Cytotoxicity assay

HeLa cells were seeded in 35 mm dishes at a density of 200,000 cells/well. One day after the incubation, PEI max, PEI max-coated MNPs, DNA, DNA/PEI max complexes, and DNA/PEI max/MNP complexes were added to each dish. The method of transfection and preparation of each MNP density was the same as that for the transfection experiment. Two days after incubation, cell viability was evaluated by trypan blue dye exclusion test.

Size measurement

The hydrodynamic sizes of the PEI max-coated γ-Fe_2O_3 and Fe_3O_4 nanoparticles were measured by dynamic light scattering (DLS) method using a fiber-optical particle analyzer (FPAR-1000, Otsuka Electronics). The morphologies of the PEI max-coated γ-Fe_2O_3 nanoparticles and DNA/PEI max/γ-Fe_2O_3 nanoparticle complexes were characterized by transmission electron microscopy (TEM).

Endocytic inhibitors

Chlorpromazine and genistein were used as endocytic inhibitors. Chlorpromazine (Nacalai Tesque) inhibits clathrin-dependent endocytosis (CDE), and genistein (Nacalai Tesque and Fujicco Co.) inhibits clathrin-independent endocytosis (CIE).

In the transfection experiment, HeLa cells (200,000 cells/well) were seeded in 35 mm dishes on the day prior to the initiation of the inhibition study. The cells were preincubated with endocytic inhibitors (10 μg/ml chlorpromazine or 200 μM genistein) in 1 ml/well of medium for 30 min. Endocytic inhibitors were also added during magnetofection and incubated for 1 h after magnetofection. Chlorpromazine was diluted in sterile water, and genistein was diluted in dimethyl sulfoxide (DMSO) so that the final concentration of DMSO in the medium was <0.1 % (Gruenstein et al. 1975; Rejman et al. 2005; Vercauteren et al. 2011).

Results and discussion

Dependency of transfection efficiency on weight of MNPs and cytotoxicity assay

Figure 1 illustrates the dependency of transfection efficiency on the weight of γ-Fe_2O_3 and Fe_3O_4 nanoparticles. Transfection efficiency increased with weight, but decreased with further increases in γ-Fe_2O_3 and Fe_3O_4 (>1.5 μg). This dependency has been reported elsewhere (Plank et al. 2003; Kami et al. 2011a). For the weight of 1.5 and 2.25 μg (γ-Fe_2O_3) and 1.5, 2.25, and 3.0 μg (Fe_3O_4), differences in transfection efficiency were not significant ($p \geq 0.05$). The transfection efficiency of γ-Fe_2O_3 nanoparticles was higher compared with that of Fe_3O_4 nanoparticles at 0.75, 1.5, and 2.25 μg ($p < 0.05$). Figure 2 is fluorescent micrographic images of γ-Fe_2O_3. These images also indicated the trend of transfection efficiency shown in Figs. 1 (2).

Figure 3 illustrates the viability of HeLa cells exposed to PEI max, PEI max-coated γ-Fe_2O_3 nanoparticles, DNA, DNA/PEI max complexes, and DNA/PEI max/γ-Fe_2O_3 nanoparticle complexes. The weight of MNPs was 2.25 μg (Fig. 3). The reduction in cell viability in cells exposed to PEI max and DNA compared with the control sample without PEI max, MNPs, or DNA was negligible ($p \geq 0.05$). The cell viability of the sample with PEI max-coated MNPs, DNA/PEI max complexes, and DNA/PEI max/MNP complexes decreased in contrast to the sample with only PEI max ($p < 0.05$). In addition, viability decreased significantly in the sample with DNA/PEI/max MNP complexes in comparison with the sample containing

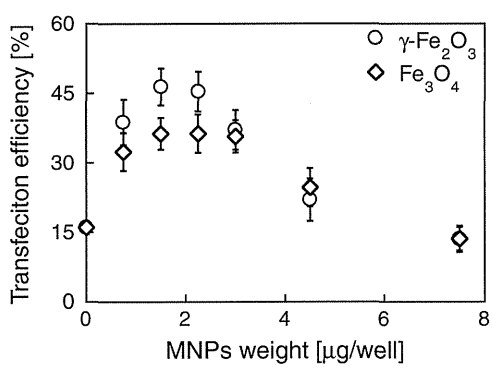

Fig. 1 Transfection efficiency as a function of magnetic nanoparticles (MNP) weight. Transfection efficiency was evaluated by fluorescent microscopy. MNP weight of 0 μg/well indicates the sample containing DNA/polyethylenimine (PEI) max complexes

only DNA ($p < 0.05$). Figure 4 illustrates the dependency of cell viability on the weight of MNPs. Cell viability initially decreased with weight of MNPs; however, it increased with further increase in MNP weight (above 2.25 μg; $p < 0.05$).

Decline in transfection efficiency has been attributed to cytotoxicity of DNA/MNPs (Plank et al. 2003). However, Figs. 1 and 4 show that cell viability in contrast to the decline in transfection efficiency, increased at higher MNP weights. In addition, the γ-Fe_2O_3 nanoparticle without coating has been reported to be of low cytotoxicity (Lee et al. 2011). It has been also reported that linear PEI has low cytotoxicity at lower concentrations, but is cytotoxic at higher concentrations (Banerjee et al. 2006; Jeong et al. 2001). In this study, the cytotoxicity of HeLa cells that were exposed to PEI max was significantly low because PEI max was used in low concentrations. Decline in cell viability in PEI max-coated γ-Fe_2O_3 nanoparticles is induced by reactive oxygen species due to the formation of free hydroxyl radical species, reacting with a range of intracellular constituents, due to high internalization of γ-Fe_2O_3 nanoparticles (McCord 1998; van der Bos et al. 2003; Arsianti et al. 2010b). However, this decline was minor because of the low doses of MNP incorporated into cells. Figures 3 and 4 suggest that the cytotoxicity may be attributed to high internalization of DNA/PEI max/MNP complexes into cells. The toxicity of DNA per se was negligible (Fig. 3). Internalization of DNA/PEI max/MNP complexes decreases cell viability, probably because of the disruption of cell membrane integrity after internalization (Prijic et al. 2012). The viability of HeLa cells exposed to complexes that contained γ-Fe_2O_3 nanoparticles of 2.25 μg was reduced despite the low cytotoxicity of PEI max-coated γ-Fe_2O_3 nanoparticles. The sample with MNPs of 2.25 μg induced higher transfection efficiency. This result suggests that cytotoxicity was because of higher internalization of DNA/PEI max/MNP complexes, and the trade-off between transfection efficiency and cytotoxicity is indicated (Arsianti et al. 2010b). The dependency of transfection efficiency and cell viability on the weight of MNPs indicates that transfection efficiency was not reduced because of cytotoxicity.

Aggregation of PEI max-coated MNPs

Figure 5 illustrates the size distribution of PEI max-coated γ-Fe_2O_3 and Fe_3O_4 nanoparticles in sterile

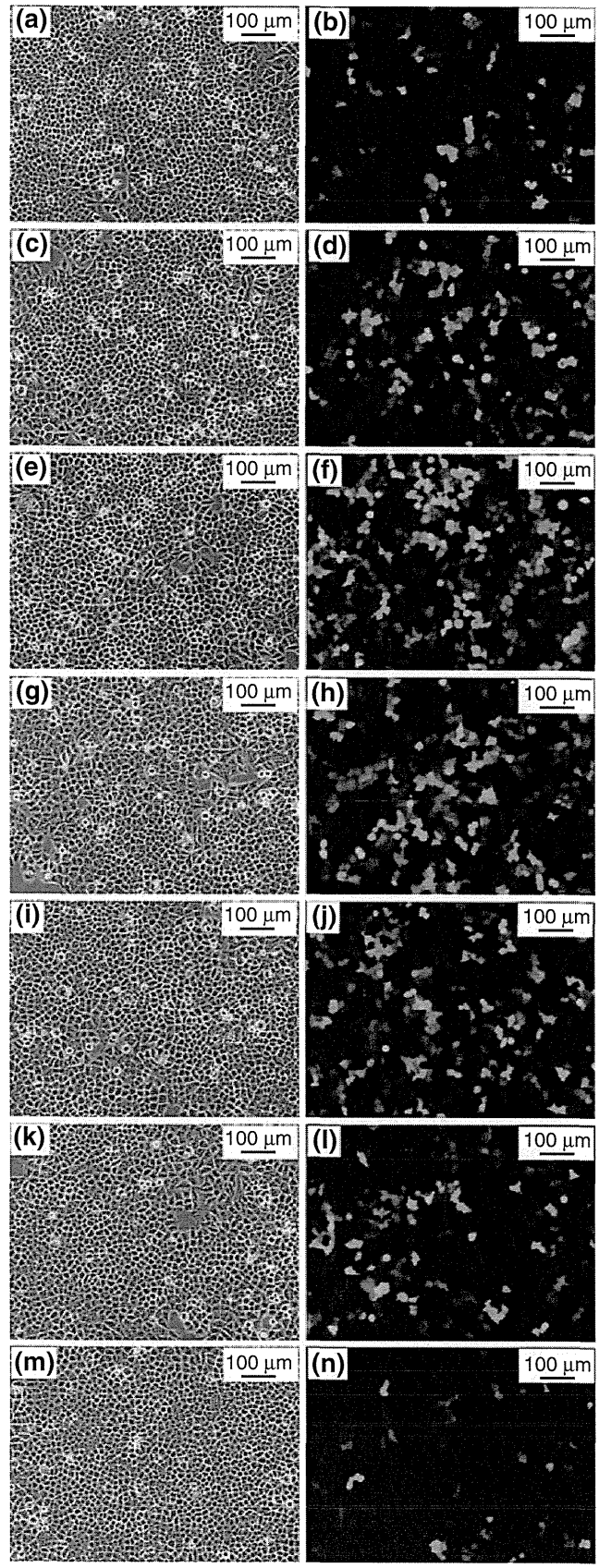

Fig. 2 Phase contrast (**a**, **c**, **e**, **g**, **i**, **k**, and **m**) and fluorescent (**b**, **d**, **f**, **h**, **j**, **l**, and **n**) micrographic images of transfected cells in the sample with γ-Fe_2O_3 of **a**, **b** 0, **c**, **d** 0.75, **e**, **f** 1.5, **g**, **h** 2.25, **i**, **j** 3.0, **k**, **l** 4.5, and **m**, **n** 7.5 μg. MNP weight of 0 μg/well indicates the sample containing DNA/polyethylenimine (PEI) max complexes

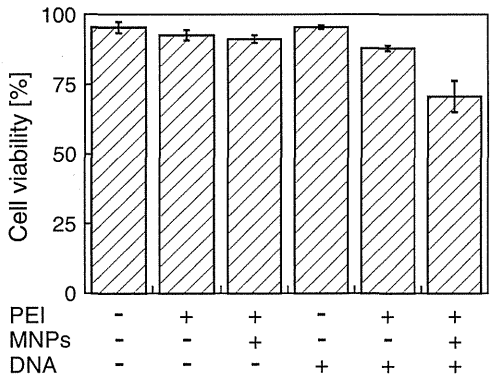

Fig. 3 Cell viability of HeLa cells in the presence of polyethylenimine (PEI) max, PEI max-coated γ-Fe_2O_3 nanoparticles, DNA, DNA/PEI max complexes, and DNA/PEI max/γ-Fe_2O_3 nanoparticle complexes. The weight of magnetic nanoparticles (MNPs) was 2.25 μg. The viability was evaluated by trypan blue dye exclusion test

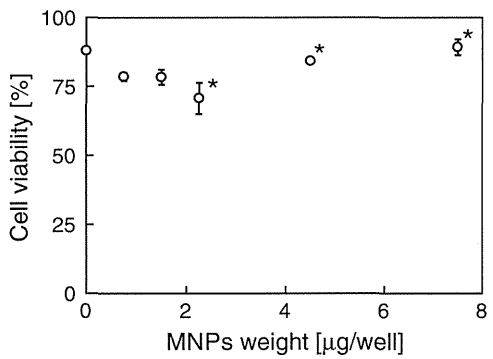

Fig. 4 Cell viability of HeLa cells as a function of the weight of polyethylenimine (PEI) max-coated γ-Fe_2O_3 nanoparticles. Magnetic nanoparticles (MNP) weight of 0 μg/well indicates the sample containing DNA/PEI max complexes. Confirmation of the dependency of cell viability on the weight of MNPs is marked with *asterisk* ($p < 0.05$)

water (Fig. 5a), DNA/PEI max/γ-Fe_2O_3 and Fe_3O_4 nanoparticle complexes in sterile water (Fig. 5b), the complexes in the medium (Fig. 5c) and pure medium, DMEM supplemented with 10 % FBS and 1 % PS (Fig. 5d) as measured by DLS. The diameters of PEI max-coated nanoparticles in sterile water were 84 ± 31 nm (γ-Fe_2O_3) and 115 ± 35 nm (Fe_3O_4). The diameters of DNA/PEI max/MNP complexes in sterile water were 126 ± 27 nm (γ-Fe_2O_3) and 116 ± 26 nm (Fe_3O_4). The diameters of the complexes in the medium were 191 ± 39 nm (γ-Fe_2O_3) and 200 ± 43 nm (Fe_3O_4). The size of the pure medium was 111 ± 27 nm. These complexes included micro-size complexes, but this finding was not considered for evaluation in this study. In sterile

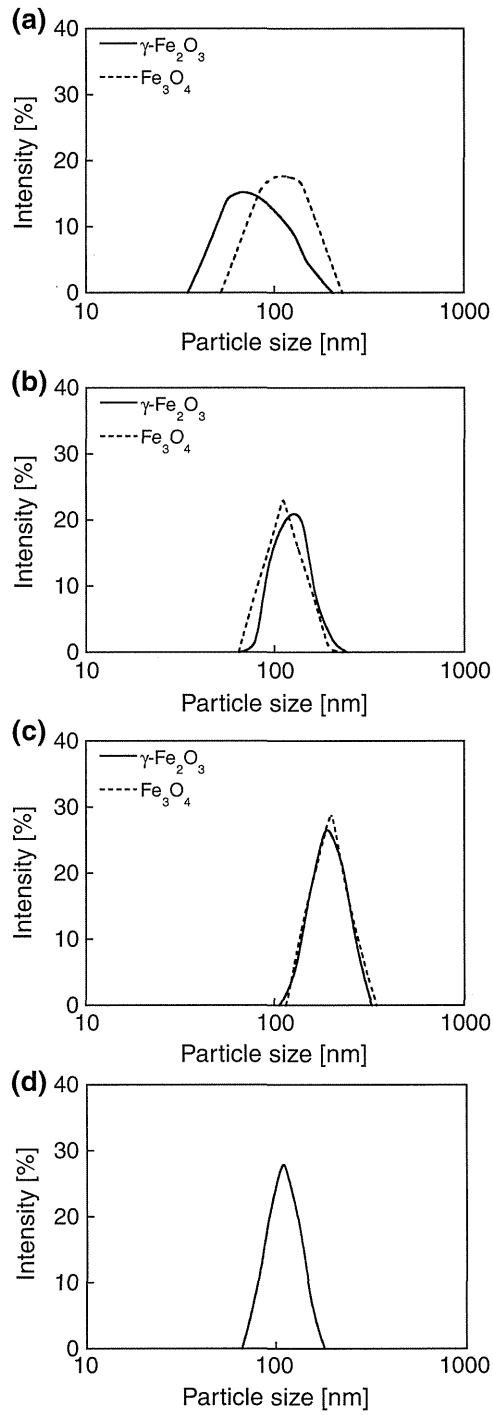

water, the size of PEI max-coated Fe_3O_4 nanoparticles is larger than that of PEI max-coated γ-Fe_2O_3 nanoparticles because the surface charge of bare Fe_3O_4 nanoparticles is lower than that of bare γ-Fe_2O_3 nanoparticles in the surface-coating process. In sterile water, bare Fe_3O_4 nanoparticles aggregate more readily than bare γ-Fe_2O_3 nanoparticles because the isoelectric point of Fe_3O_4 is nearer to the pH of sterile

◀**Fig. 5** Size distribution of **a** polyethylenimine (PEI) max-coated γ-Fe_2O_3 and Fe_3O_4 nanoparticles in sterile water, **b** DNA/PEI max/γ-Fe_2O_3 and Fe_3O_4 nanoparticle complexes in sterile water, **c** DNA/PEI max/γ-Fe_2O_3 and Fe_3O_4 nanoparticle complexes in medium, and **d** pure medium (Dulbecco's modified Eagle medium supplemented with 10 % FBS and 1 % PS) as measured by dynamic light scattering (DLS). **b** and **c** were compared in the same condition as the ratio of DNA, PEI max, and magnetic nanoparticles (MNPs) to each other. The sizes were **a** 84 ± 31 nm (γ-Fe_2O_3), 115 ± 35 nm (Fe_3O_4), **b** 126 ± 27 nm (γ-Fe_2O_3), 116 ± 26 nm (Fe_3O_4), **c** 191 ± 39 nm (γ-Fe_2O_3), 200 ± 43 nm (Fe_3O_4), and **d** 111 ± 21 nm. The complexes contained particles of micro-size, but this finding was not considered for evaluation in this study

water (pH 7.0) than that of γ-Fe_2O_3. Aggregation of PEI max-coated γ-Fe_2O_3 nanoparticles induced by DNA binding was confirmed (Fig. 5a, b). PEI max-coated Fe_3O_4 nanoparticles also aggregated because the complexes (both γ-Fe_2O_3 and Fe_3O_4) were of microsize (data not shown). PEI max-coated MNPs aggregate because of DNA binding. TEM observations also show that PEI max-coated MNPs aggregate because of conjugation with DNA (Fig. 6). Moreover, the medium induces additional aggregation of the complexes (Fig. 5b, c). The pH of culture medium is 7.4 (mildly alkaline), whereas that of sterile water is 7.0 (neutral). The positive surface charge of PEI-coated MNPs decreases owing to the mildly alkaline pH of the solvent. The complexes conjugate with serum protein contained in the medium. However, it has been reported that serum protein prevents the aggregation of MNPs modified with polymers (Wigo et al. 2012). The aggregation of the complexes in this study was reduced compared with serum-free medium because of serum proteins (data not shown).

A decrease in electrostatic repulsion due to DNA binding and mildly alkaline pH in the medium (pH 7.4) has been reported to induce aggregation of complexes (Arsianti et al. 2010a; Kami et al. 2011b; Miao et al. 2013). An increase in pH to a mildly alkaline level contributed to the instability of PEI-coated MNPs (Steitz et al. 2007; Wang et al. 2009). The models of aggregation for both γ-Fe_2O_3 and Fe_3O_4 nanoparticles are very similar.

Dependency of aggregation of DNA/PEI max/MNP complexes on weight of MNPs in the medium

Figures 7 and 8 illustrate the size distribution of the DNA/PEI max/γ-Fe_2O_3 and Fe_3O_4 nanoparticle complexes in the medium for weight of each of the MNPs as measured by DLS. The diameters of the γ-Fe_2O_3 complexes were 127 ± 27, 124 ± 24, 175 ± 41, and 191 ± 39 nm for samples with weights of 0.75, 2.25, 4.5, and 7.5 μg, respectively. The diameters of the Fe_3O_4 complexes were 141 ± 30, 144 ± 30, 152 ± 30, and 200 ± 43 nm for the samples with the weight of 0.75, 2.25, 4.5, and 7.5 μg, respectively. The samples contained micro-size complexes, but this finding was not considered for evaluation in this study. The size distributions indicated that aggregation was due to high weight of MNPs, except in the samples of 0.75 and 2.25 μg as confirmed for γ-Fe_2O_3 and Fe_3O_4 complexes. This result indicates that the concentration of MNPs in the medium influences the aggregation of the complexes and that higher concentration induces higher aggregation. This aggregation affects transfection efficiency, which depends on the weight of MNPs (Fig. 1). The differences in transfection efficiency between γ-Fe_2O_3 and Fe_3O_4 are also influenced by the size of complexes. However, comparison of transfection efficiency between nanoparticles such as γ-Fe_2O_3 and Fe_3O_4 must take into account magnetization as a factor, influencing magnetic force on the particles (Johnson et al. 1975; Pankfurst et al. 2003; Furlani and Xue 2012).

In addition, the number of DNA/PEI max/MNP complexes was estimated by the following equation:

$$N = \frac{M}{VP} \tag{1}$$

where N is the number of complexes, M is the weight of MNPs used in each condition, V is the volume of complexes, and P is the bulk density of the MNPs. The volume was estimated by the following equation on the basis of the size distribution:

$$V = \sum_{k=1}^{n} \frac{4}{3}\pi\left(\frac{D_k}{2}\right)^3 F_k \tag{2}$$

where D is the diameter of the complexes, F is the fraction of the complexes of each diameter, and n is the number of measurement points. This estimate is rough because the complexes are not perfect spheres. However, this estimate gives excellent insight into the influence of MNP weight on transfection efficiency. The number of complexes decreased with increasing sizes of the complexes and the sizes

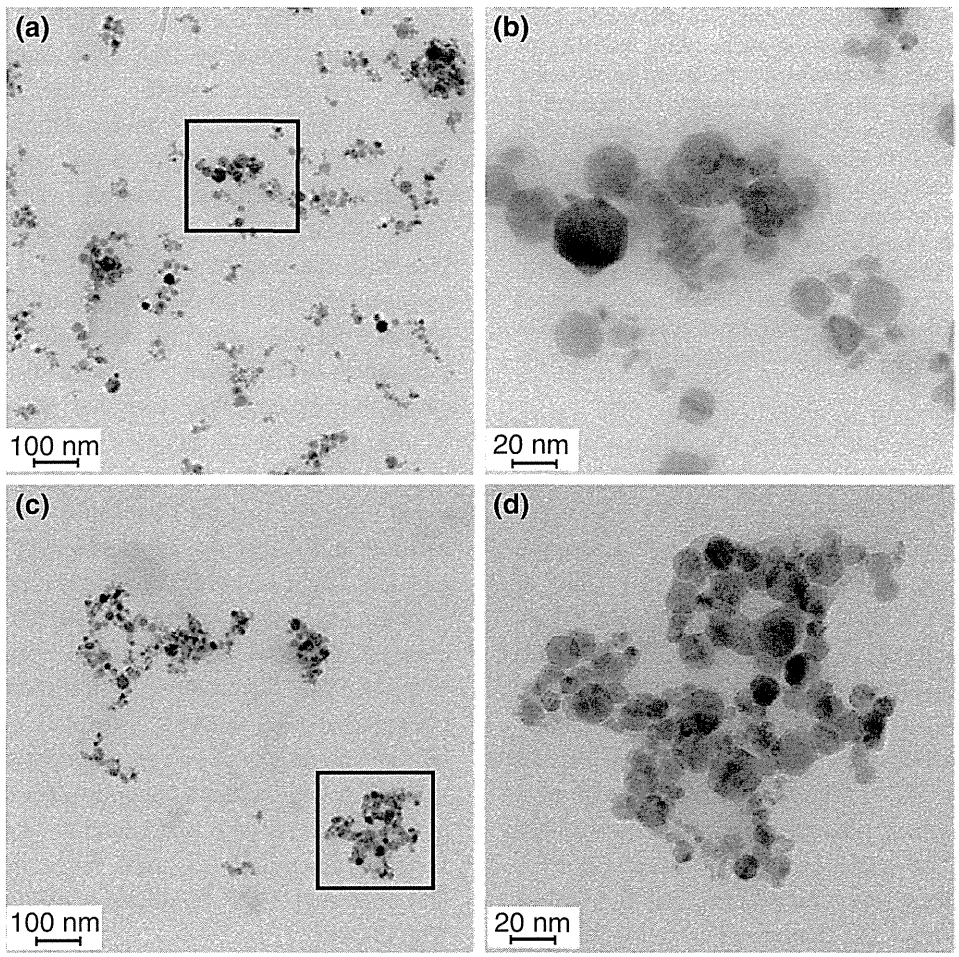

Fig. 6 Transmission electron microscopy (TEM) images of **a** polyethylenimine (PEI) max-coated magnetic nanoparticles (MNPs) (γ-Fe_2O_3 nanoparticles), **b** PEI max-coated MNPs magnified from **a**, **c** DNA/PEI max/MNP (2.25 μg/well γ-Fe_2O_3 nanoparticle) complexes, **d** DNA/PEI max/MNP complex magnified from **c**. These were observed in sterile water. These images show that the complexes were larger than the PEI max-coated MNPs

increased because of aggregation. Figure 9 illustrates that the trend of transfection efficiency is according to the number of γ-Fe_2O_3 complexes. The number of complexes of size up to 200 nm was indicated by this estimate because higher internalization is confirmed to be achieved with nanoparticles of size up to 200 nm (Rejman et al. 2004). This trend was also confirmed for Fe_3O_4 complexes (data not shown). It is possible that aggregation affects transfection efficiency because of cellular uptake inhibition and reduction in the number of complexes.

Endocytic pathways of DNA/PEI max/MNP complexes

The endocytic pathways of the DNA/PEI/MNP complexes were similar to those of PEI polyplexes (Huth et al. 2004). Endocytosis is divided into phagocytosis (the uptake of large particles) and pinocytosis (the uptake of fluids and solutes). Pinocytosis is classified into clathrin-dependent endocytosis (CDE) and clathrin-independent endocytosis (CIE) (Sahay et al. 2010). Nanoparticles with diameter up to 200 nm are internalized by CDE (Rejman et al. 2004), whereas nanoparticles that are not internalized by CDE enter the cells by CIE, for example caveolae- and flotillin-dependent endocytosis (Rejman et al. 2004; Payne et al. 2007). Flotillin-dependent endocytosis is PEI receptor (proteoglycan)-mediated pathway (Zanta et al. 1997; Zou et al. 2000), and proteoglycan is known as cell surface receptor binding cationic substrates (Mislick and Baldeschwieler 1996). Receptor-mediated endocytosis is induced by interaction between ligand and receptor bound to the cell surface.

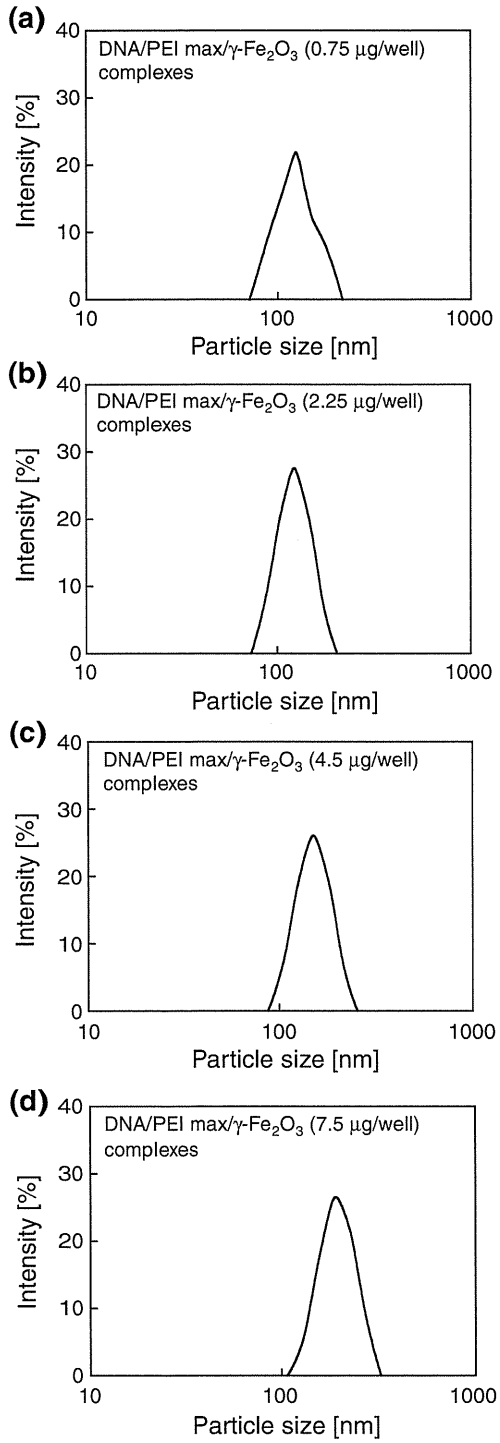

Fig. 7 Size distribution of DNA/polyethylenimine (PEI) max/γ-Fe_2O_3 nanoparticle complexes in medium, as measured by dynamic light scattering (DLS) for **a** 0.75 μg/well, **b** 2.25 μg/well, **c** 4.5 μg/well, and **d** 7.5 μg/well, and the sizes of the complexes were **a** 127 ± 27 nm, **b** 124 ± 24 nm, **c** 152 ± 30 nm, **d** 191 ± 39 nm, respectively. The samples contained micro-order size complexes, but this finding was not considered for evaluation in this study

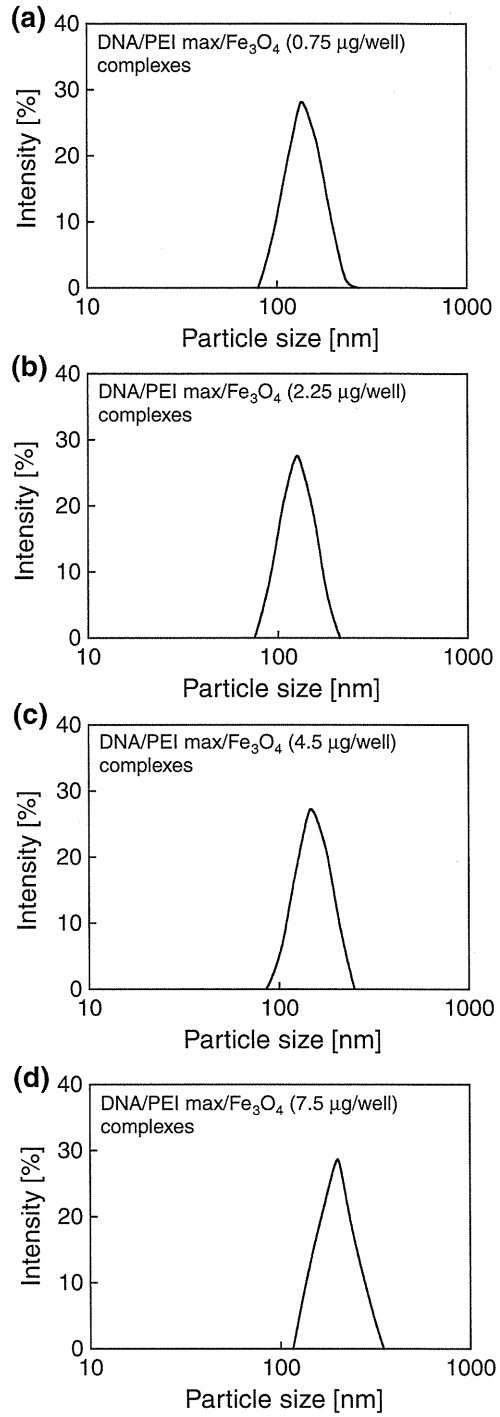

Fig. 8 The size distribution of DNA/polyethylenimine (PEI) max/Fe_3O_4 nanoparticle complexes in the medium as measured by dynamic light scattering (DLS) for **a** 0.75 μg/well, **b** 2.25 μg/well, **c** 4.5 μg/well, **d** 7.5 μg/well, and the size of the complexes were **a** 141 ± 30 nm, **b** 144 ± 30 nm, **c** 152 ± 30 nm, **d** 200 ± 43 nm, respectively. The samples contained micro-order size complexes, but this finding was not considered for evaluation in this study

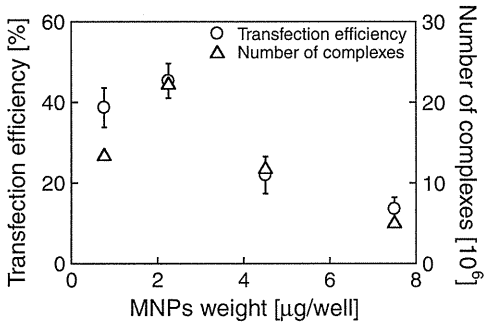

Fig. 9 The number of DNA/polyethylenimine (PEI) max/magnetic nanoparticles (MNP) complexes assessed on the basis of size distribution compared with the transfection efficiency. The trend in transfection efficiency corresponds to the numbers of complexes

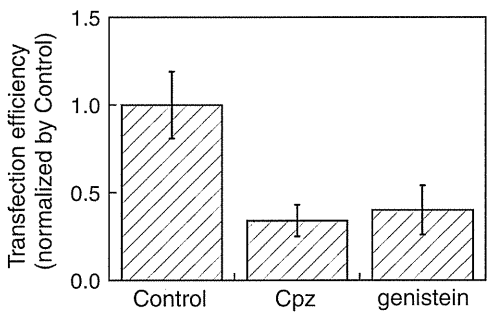

Fig. 10 Effects of inhibitors on the transfection efficiency of γ-Fe2O3 nanoparticles (control: inhibitor-free, Cpz: addition of chlorpromazine, genistein: addition of genistein). 10 μg/ml chlorpromazine or 200 μM genistein was added

With respect to receptor-mediated endocytosis, the model of endocytosis for efficient internalization has been reported (Gao et al. 2005; Decuzzi and Ferrari 2007; Lunov et al. 2011). Wrapping time, and threshold and optimal radii of particles are important factors for particle endocytosis. These factors can be represented as the function of receptor/ligand density ratio and estimated by receptor/ligand binding energy factor, bond elasticity factor, and non-specific attractive/repulsive factor at cell/particle interface (Gao et al. 2005; Decuzzi and Ferrari 2007). Moreover, wrapping time is also represented as the function of the forces acting on particle captured by receptors, which contain the elastic forces of the cellular membrane and the internal forces of receptor (Lunov et al. 2011). The optical radius of particles is estimated from wrapping time, cell lateral size, and the number of nanoparticles captured per second (Lunov et al. 2011). Optimal size of nanoparticle is up to 50 nm for efficient internalization by receptor-mediated endocytosis (Gao et al. 2005). On the other hand, in vitro test has indicated that nanoparticle with diameter up to 100–200 nm is optimal (Win and Feng 2005). Therefore, the estimation for efficient internalization must take into account the factors influenced on particle configuration, coating agent, cell type, and cultural environment.

Figure 10 illustrates the transfection rate for DNA/PEI max/MNP (γ-Fe_2O_3 of 2.25 μg) complexes in the presence of chlorpromazine as a CDE inhibitor and genistein as a CIE inhibitor. The transfection rate was decreased by both endocytic inhibitors, showing that the complexes were internalized by CDE and CIE. This result agrees with those of previous studies (Huth et al. 2004). DNA/PEI max/MNP complexes are internalized by CDE and caveolae- and flotillin-dependent endocytosis, which are classified as CIE because cellular internalization of polyplexes through these endocytic pathways has been confirmed (Huth et al. 2004; Rejman et al. 2005; Payne et al. 2007; Vercauteren et al. 2011). It is indicated that the efficient internalization of the complexes depends on the size of the complexes and other factors such as the number of complexes and the ligand/receptor interactions between PEI and PEI receptors on cell surfaces.

Conclusion

Magnetofection using DNA/PEI max/MNP complexes was studied. Transfection efficiency was enhanced using MNPs and an applied magnetic field, but it decreased with high weight of MNPs despite the increase in cell viability. DNA/PEI max/MNP complexes aggregated because of alkaline pH of the medium and the reduction in electrostatic repulsion induced by DNA binding. The sizes of the complexes increased with high weight of MNPs in the medium. Aggregation induced by high weight of MNPs inhibited cellular uptake by size-dependent endocytosis and led to a decline in the number of complexes. The decline of transfection efficiency in high weight of MNPs was due to aggregation of the complexes; therefore, it was concluded that this decline was not due to cytotoxicity.

References

Akincl A, Thomas M, Klibanov AM, Langer R (2005) Exploring polyethylenimine-mediated DNA transfection and the proton sponge hypothesis. J Gene Med 7:657–663

Akiyama H, Ito A, Kawabe Y, Kamihira M (2010) Genetically engineered angiogenic cell sheets using magnetic force-based gene delivery and tissue fabrication techniques. Biomaterials 31:1251–1259

Arsianti M, Lim M, Marquis CP, Amal R (2010a) Assembly of polyethylenimine-based magnetic iron oxide vectors: insight into gene delivery. Langmuir 26:7314–7326

Arsianti M, Lim M, Marquis CO, Amal R (2010b) Polyethylenimine based magnetic iron-oxide vector: the effect of vector component assembly on cellular entry mechanism, intracellular localization, and cellular viability. Biomacromolecules 11:2521–2531

Banerjee P, Weissleder R, Bogdanov A Jr (2006) Linear polyethylenimine grafted to a hyperbranched poly(ethylene glycol)-like core: a copolymer for gene delivery. Bioconjug Chem 17:125–131

Boussif O, Lezoualc'h F, Zanta MA, Mergny MD, Scherman D, Demeneix B, Behr J (1995) A versatile vector for gene and oligonucleotide transfer into cells in culture and in vivo: polyethylenimine. Proc Natl Acad Sci USA 92:7297–7301

De Smedt SC, Demeester J, Hennink WE (2000) Cationic polymer based gene delivery systems. Pharm Res 17: 113–126

Decuzzi P, Ferrari M (2007) The role of specific and non-specific interactions in receptor-mediated endocytosis of nanoparticles. Biomaterials 28:2915–2922

Furlani EP, Xue X (2012) Field, force and transport analysis for magnetic particle-based gene delivery. Microfluid Nanofluidics 13:589–602

Gao H, Shi W, Freund LB (2005) Mechanism of receptor-mediated endocytosis. Proc Natl Acad Sci USA 102:9469–9474

Ghosh PS, Kim C, Han G, Forbes NS, Rotello VM (2008) Efficient gene delivery vectors by tuning the surface charge density of amino acid-functionalized gold nanoparticles. ACS Nano 2:2213–2218

Godbey WT, Wu KK, Mikos AG (1999) Poly(ethylenimine) and its role in gene delivery. J Control Release 60:149–160

Gruenstein E, Rich A, Weihing RR (1975) Actin associated with membranes from 3T3 mouse fibroblast and HeLa cells. J Cell Biol 64:223–234

Guo X, Kim KS, Liu D (2007) Nonviral gene delivery: what we know and what is next. AAPS J 9:E92–E104

Huth S, Lausier J, Gersting SW, Rudolph C, Plank C, Welsch U, Rosenecker J (2004) Insight into the mechanism of magnetofection using PEI-based magnetofection for gene transfer. J Gene Med 6:923–936

Jeong JH, Song DH, Lim DW, Lee H, Park TG (2001) DNA transfection using poly(ethylenimine) prepared by controlled acid hydrolysis of poly(2-ethyl-2-oxazoline). J Control Release 73:391–399

Johnson HP, Lowrie W, Kent DV (1975) Stability of anhysteretic remanent magnetization in fine and coarse magnetite and maghemite particles. Geophys J R Astr Soc 41:1–10

Kami D, Takeda S, Makino H, Toyoda M, Gojo S, Kyo S, Umezawa A, Watanabe M (2011a) Efficient transfection method using deacylated polyethylenimine-coated magnetic nanoparticles. J Artif Organs 14:215–222

Kami D, Takeda S, Toyoda M, Watanabe M (2011b) Application of magnetic nanoparticles to biomedicine. Int J Mol Sci 11:3705–3722

Kichler A, Leborgne C, Coeytaux E, Danos O (2001) Polyethylenimine-mediated gene delivery: a mechanistic study. J Gene Med 3:135–144

Kievit FM, Veiseh O, Bhattarai N, Fang C, Gunn JW, Lee D, Ellenbogen RG, Olson JM, Zhang M (2009) PEI–PEG–chitosan copolymer coated iron oxide nanoparticles for safe gene delivery: synthesis, complexation, and transfection. Adv Funct Mater 19:2244–2251

Kircheis R, Wightman L, Wagner E (2001) Design and gene delivery activity of modified polyethylenimines. Adv Drug Deliv Rev 53:341–358

Lee KJ, An JH, Shin JS, Kim DH, Yoo HS, Cho CK (2011) Biostability of γ-Fe_2O_3 nano particles evaluated using an in vitro cytotoxicity assays on various tumor cell lines. Curr Appl Phys 11:467–471

Lunov O, Zablotskii V, Syrovets T, Röcker C, Tron K, Nienhaus GU, Simmet T (2011) Modeling receptor-mediated endocytosis of polymer-functionalized iron oxide nanoparticles by human macrophage. Biomaterials 32:547–555

McCord JM (1998) Iron free radicals, and oxidative injury. Semin Hematol 35:5–12

Miao L, Zhang K, Oiao C, Jin X, Zhang C, Yang B, Sun H (2013) Antitumor effect of human TRAIL on adenoid cystic carcinoma using magnetic nanoparticle–mediated gene expression. Nano-medicine 9:141–150

Mislick KA, Baldeschwieler JD (1996) Evidence for the role of proteoglycans in cation-mediated gene transfer. Proc Natl Acad Sci USA 93:12349–12354

Oku N, Yamazaki Y, Matsuura M, Sugiyama M, Hasegawa M, Nango M (2001) A novel non-viral gene transfer system, polycation liposomes. Adv Drug Deliv Rev 52:209–218

Pan B, Cui D, Sheng Y, Ozkan C, Gao F, He R, Li Q, Xu P, Huang T (2007) Dendrimer-modified magnetic nanoparticles enhance efficiency of gene delivery system. Cancer Res 67:8156–8163

Pankfurst QA, Connolly J, Jones SK, Dobson J (2003) Applications of magnetic nanoparticles in biomedicine. J Phys D 36:R167–R181

Payne CK, Jones SA, Chen CC, Zhuang X (2007) Internalization and trafficking of cell surface proteoglycans and proteoglycan-binding ligand. Traffic 8:389–401

Plank C, Schillinger U, Scherer F, Bergemann C, Rémy JS, Kröetz F, Anton M, Lausier J, Rosenecker J (2003) The magnetofection method: using magnetic force to enhance gene delivery. Biol Chem 384:737–747

Prabha S, Zhou WZ, Panyam J, Labhastwar V (2002) Size-dependent of nanoparticle-mediated gene transfection: studies with fractionated nanoparticles. Int J Pharm 244:105–115

Prijic S, Prosen L, Cemazar M, Scancar J, Romih R, Lavrencakv J, Bregar VB, Coer A, Krzan M, Znidarsic A, Sersa G (2012) Surface modified magnetic nanoparticles for immuno-gene therapy of murine mammary adenocarcinoma. Biomaterials 233:4379–4391

Rejman J, Oberle V, Zuhorn IS, Hoekstr D (2004) Size-dependent internalization of particles via the pathways of clathrin-and caveolae-mediated endocytosis. Biochem J 377:159–169

Rejman J, Bragonzi A, Conese M (2005) Role of clathrin- and caveolae-mediated endocytosis in gene transfer mediated by lipo- and polyplexes. Mol Ther 12:468–474

Roy I, Ohulchanskyy TY, Bharali DJ, Pudavar HE, Mistretta RA, Kaur N, Prasad PN (2005) Optical tracking of organically modified silica nanoparticles as DNA carriers: a nonviral, nanomedicine approach for gene delivery. Proc Natl Acad 102:279–284

Sahay G, Alakhova DY, Kabanov AV (2010) Endocytosis of nanomedicines. J Control Release 145:182–195

Scherer F, Anton M, Schillinger U, Henke J, Bergemann C, Krüger A, Gänsbacher B, Plank C (2002) Magnetofection: enhancing and targeting gene delivery by magnetic force in vitro and in vivo. Gene Ther 9:102–109

Seino S, Matsuoka Y, Kinoshita T, Nakagawa T, Yamamoto TA (2009) Dispersibility improvement of gold/iron-oxide composite nanoparticles by polyethylenimine modification. J Magn Magn Mater 321:1404–1407

Steitz B, Hofmann H, Kamau SW, Hassa PO, Hottiger MO, Rechenberg B, Hofmann-Amtenbrink M, Petri-Fink A (2007) Characterization of PEI-coated superparamagnetic iron oxide nanoparticles for transfection: size distribution, colloidal properties and DNA interaction. J Magn Magn Mater 311:300–305

Thomas M, Lu JJ, Ge Q, Zhang C, Chen J, Klibanov AM (2005) Full deacylation of polyethylenimine dramatically boosts its gene delivery efficiency and specificity to mouse lung. Proc Natl Acad Sci USA 102:5679–5684

van den Bos EJ, Wagner A, Mahrholdt H, Thompson RB, Morimoto Y, Sutton BS, Judd RM, Taylor DA (2003) Improved efficacy of stem cell labeling for magnetic resonance imaging studies by the use of cationic liposomes. Cell Transplant 12:743–756

Vercauteren D, Piest M, van der Aa LJ, Al Soraj M, Jones AT, Engbersen JF, De Smedt SC, Braeckmans K (2011) Flotillin-dependent endocytosis and a phagocytosis-like mechanism for cellular internalization of disulfide-based poly(amido amine)/DNA polyplexes. Biomaterials 32:3072–3084

Wang X, Zhou L, Ma Y, Li X, Gu H (2009) Control of aggregation size of polyethylenimine-coated magnetic nanoparticles for magnetofection. Nano Res 2:365–372

Wang S, Lee C, Chiou A, Wei P (2010) Size-dependent endocytosis of gold nanoparticles studied by three-dimensional mapping of plasmonic scattering images. J Nanobiotech 8:33

Wigo HTR, Lim M, Bulmus V, Gutiérrez L, Woodward RC, Amal R (2012) Insight into serum protein interactions with functionalized magnetic nanoparticles in biological media. Langmuir 28:4346–4356

Win KY, Feng S (2005) Effects of particle size and surface coating on cellular uptake of polymeric nanoparticles for oral delivery of anticancer drugs. Biomaterials 26: 2713–2722

Zanta M, Boussif O, Adib A, Behr J (1997) *In vitro* gene delivery to hepatocytes with galactosylated polyethylenimine. Bioconjug Chem 8:839–844

Zou S, Erbacher P, Remy JS, Behr J (2000) Systemic linear polyethylenimine (L-PEI)-mediated gene delivery in the mouse. J Gene Med 2:128–134

Self-Heating Temperature and AC Hysteresis of Magnetic Iron Oxide Nanoparticles and Their Dependence on Secondary Particle Size

Kosuke Nakamura[1], Koji Ueda[1], Asahi Tomitaka[2], Tsutomu Yamada[1], and Yasushi Takemura[1]

[1]Department of Electrical and Computer Engineering, Yokohama National University, Yokohama, 240-8501, Japan
[2]Department of Materials Science and Engineering, University of Washington, Seattle, WA 98195 USA

Magnetic nanoparticles are expected to be used as hyperthermia agents. The mechanism of self-heating of the magnetic nanoparticles under an ac magnetic field is different according to their size. In this study, the temperature rise for the ac/dc hysteresis loops of magnetic nanoparticles were evaluated to clarify the contribution of the Néel and Brownian relaxations to heat dissipation. The samples were dextran-coated magnetic iron oxide nanoparticles of different hydrodynamic diameters (40, 54, and 86 nm), but the same primary diameter of 10 nm. From these diameters, the peak frequencies for the Brownian and Néel relaxations were calculated. The Néel relaxation time, determined by the primary particle size, is much shorter than the Brownian relaxation time for these samples. Although the Néel relaxation is dominant, the self-heating temperature rise of the 86 nm sample was higher than that of the 40 and 54 nm samples. These results suggest that the effect of the magnetic interaction between the nanoparticles depends on the hydrodynamic diameter.

Index Terms—**Hyperthermia, magnetic relaxation, superparamagnetic nanoparticles.**

I. Introduction

MAGNETIC nanoparticles have received growing interest in the biological and medical application fields. For example, they can be used as heating agents for hyperthermia. With magnetic nanoparticles, the tumor can be killed by adjusting only the temperature in the vicinity of the tumor to 42.5 degrees (causing localized hyperthermia), and thus, the side effects of current treatments can be decreased [1]. It is known that magnetic nanoparticles transform the energy of an ac field into heat by several physical mechanisms, and the specific mechanism for heat generation is different depending on the particle size. That is, with large particles (on the order of microns or more), there is a multi-domain ground state that leads to a narrow hysteresis loop because it takes relatively little magnetic field energy to make the domain walls move compared to the energy required to rotate the magnetic moment of the particle. On the other hand, in smaller particles, there is a single-domain ground state that leads to a broad hysteresis loop [2]. At even smaller sizes (on the order of tens of nanometers or less), superparamagnetism can be observed that has no hysteresis loop because the magnetic moment of the particle as a whole is oscillating in response to the thermal energy at room temperature [3], [4]. Therefore, superparamagnetic nanoparticles exhibit heat dissipation under an ac magnetic field due to magnetic relaxation loss.

The heat dissipation of superparamagnetic nanoparticles is due to the delay in relaxation of the magnetic moment. This relaxation can correspond either to the physical rotation of the particles themselves within the fluid, or the rotation of the magnetic moments within each particle. The rotation of the particles is referred to as Brownian relaxation, whereas the rotation of the magnetic moment within each particle is known as Néel relaxation. The Brownian (τ_B) and Néel (τ_N) relaxation times are given by the following equations:

TABLE I
Parameters for the Magnetic Iron Oxide Nanoparticles Dispersed in Water, Including the Primary Particle Diameter $2r$, the Hydrodynamic Diameter $2r_h$, Viscosity of the Water η, Absolute Temperature T, and Magnetic Anisotropic Constant K

$2r$ [nm]	$2r_h$ [nm]	η [Pa·s]	T[K]	K [J/m^3]
10	40, 54, 86	8.9×10^{-4}	300	3×10^4

$$\tau_B = \frac{4\pi r_h^3}{k_B T}\eta \tag{1}$$

$$\tau_N = \tau_0 \exp\left(\frac{4\pi r^3 K}{3k_B T}\right) \tag{2}$$

$$\tau = \frac{\tau_N \tau_B}{\tau_N + \tau_B} \tag{3}$$

where τ is the effective relaxation time, r_h is the hydrodynamic particle diameter, η is the viscosity, k_B is Boltzmann's constant, T is the temperature, $\tau_0 = 10^{-9}$ s, r is the particle diameter, and K is the anisotropy constant [5]. These parameters are summarized in Table I. From the above equations, it is evident that the relaxation time relies on the particle diameter. When the relaxation time of the particles is longer than the period of the applied ac magnetic field, the particles exhibit heat dissipation because the rotation of the magnetic moment lags behind the changing applied magnetic field. The heat dissipation on account of magnetic relaxation loss is given by the following equations [6]:

$$P = \pi \mu_0 \chi'' H^2 f \tag{4}$$

$$\chi'' = \frac{2\pi f \tau}{1 + (2\pi f \tau)^2}\chi_0 \tag{5}$$

where P is the heat dissipation value, μ_0 is the permeability of vacuum, χ'' is the imaginary component of the susceptibility, H is the intensity of the applied ac magnetic field, f is the frequency of the applied ac magnetic field, and χ_0 is the initial magnetic susceptibility.

Manuscript received October 09, 2012; revised October 21, 2012; accepted October 21, 2012. Corresponding author: K. Nakamura (e-mail: nakamura-kosuke-vj@ynu.ac.jp).

Color versions of one or more of the figures in this paper are available online at http://ieeexplore.ieee.org.

Digital Object Identifier 10.1109/TMAG.2012.2226567

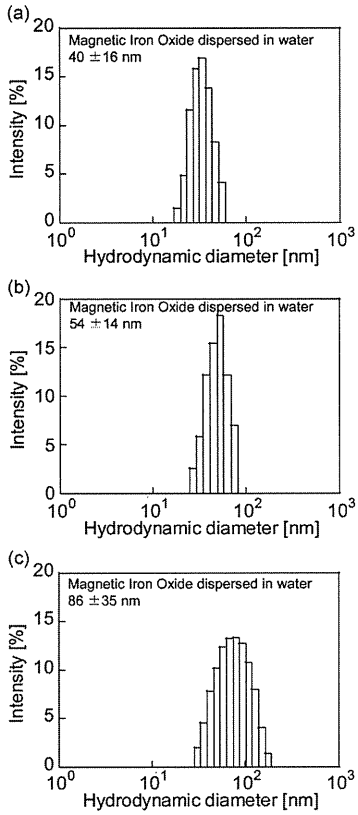

Fig. 1. Hydrodynamic diameters of dextran-coated magnetic iron oxide nanoparticles measured by dynamic laser scattering (DLS). The average hydrodynamic diameters were (a) 40 nm, (b) 54 nm, and (c) 86 nm, respectively.

The value of τ is calculated using (1)–(3) with the primary and secondary particle diameters. Therefore, the tendency of the theoretical χ'' is a function of frequency.

The self-heating property of magnetic iron oxide nanoparticles was evaluated in this study by measuring the magnetization curves and their magnetic susceptibility under an ac magnetic field. The heat-generation mechanism of magnetic particles has been clarified by measuring the magnetic susceptibility under an ac magnetic field. However, there are very few reports on the ac hysteresis curves, and they were measured at several kHz [7], [8]. A previous study reported the measurement of the hysteresis curve at a higher frequency of several hundred kHz [9]. In this study, the temperature rise and both the ac and dc hysteresis curves of the magnetic nanoparticles were evaluated in order to clarify the contribution of the Néel and Brownian relaxations to heat dissipation.

To be useful as heating agents for *in vivo* hyperthermia, excitation of the magnetic nanoparticles must occur at a low frequency and low magnetic field intensity. Therefore, the efficiency of heat dissipation (heat value per cycle) was evaluated under an ac magnetic field of 50 Oe at 50–500 kHz.

II. Sample Preparation

Three commercially available samples of magnetic iron oxide magnetic nanoparticles (Micromod GmbH) were used in this study. The samples were dextran coated to adjust their hydrodynamic diameters (40, 54, and 86 nm), which were measured by dynamic light scattering (DLS), as shown in Fig. 1. Dynamic fluctuation of the intensity of the scattered light from the particles in Brownian motion is analyzed by the autocorrelation function, which is known as the photon correlation spectroscopy technique. The histogram of hydrostatic diameter is obtained by using Levenberg-Marquardt algorism. The primary diameter was 10 nm for all three samples.

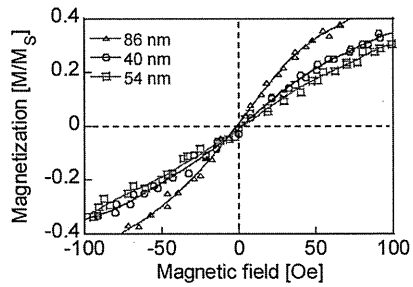

Fig. 2. Parts of major hysteresis loops of the magnetic iron oxide samples dispersed in water measured using a vibrating sample magnetometer (VSM). This figure indicates that all three samples are superparamagnetic. The magnetization is normalized by the saturation magnetization (M_s).

The dc hysteresis curves of the samples dispersed in water were measured using a vibrating sample magnetometer (VSM). The samples exhibited superparamagnetic characteristics because of their sigmoidal and anhysteretic curves (Fig. 2).

III. Experiment

The efficiency of heat dissipation was estimated by two different experimental techniques. The increase in the self-heating temperature of the sample was measured, and the specific absorption rate (SAR) was calculated using the following [10], [11]:

$$SAR = \frac{\Delta T}{\Delta t} \cdot \frac{m_p c_p + m_W c_W}{m_P} \left[\frac{\mathrm{W}}{\mathrm{g}}\right] \tag{6}$$

where m_p and m_w are the masses of the particles and the water in which the particles are distributed, respectively, and c_p and c_w are the specific heats of the particles and the water, respectively.

SAR is proportional to the slope of the initial increase in temperature. The temperature rise at initial ten seconds was used to calculate the slope, $\Delta T/\Delta t$. The efficiency of heat dissipation was calculated by dividing the value of SAR by the applied field frequency.

The temperature rise was determined by measuring the frequency over the range 50–500 kHz under an ac magnetic field of 50 Oe. The resonant circuit further consisted of a 70-turn water-cooled solenoid with a 1.76 cm diameter (a round-bottom shaped 2 ml polypropylene tube was used). The liquid sample of 1.5 ml at a concentration of 50 mg/ml in the tube was set inside the coil. The temperature of the sample was measured by using an optical fiber thermometer. The effect of the sample with respect to ambient heating from the coil was validated.

The ac hysteresis curve was measured under the same conditions as those used for the temperature-rise measurement. A glass tube ($\phi = 1.5$ mm) was used as the sample holder. The area of the hysteresis curve was calculated by determining the integral of the magnetization over all of the values of the magnetic field intensity, and was identified as the heat value per cycle of the alternating magnetic field. The resonant circuit further consisted of an 80-turn water-cooled solenoid with a 1.63 cm diameter.

To check the validity of the measurement of the ac hysteresis curves for our system, the measurement of $\gamma - Fe_2O_3$ (Resovist) was performed. Fig. 3 shows dc and ac minor hysteresis loops. The magnetization curve traced with applying a dc field

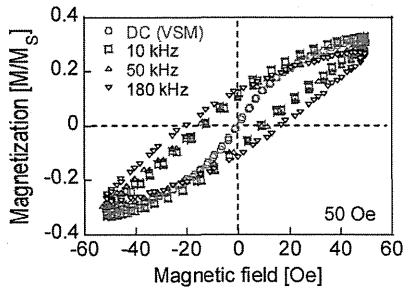

Fig. 3. DC and ac minor hysteresis loops of Resovist ($\gamma - Fe_2O_3$) measured under magnetic field of 50 Oe. The magnetization is normalized by the saturation magnetization (M_s).

indicated that the sample exhibited superparamagnetic feature with no hysteresis area. The hysteresis curves were obtained by applying ac magnetic fields at 10, and 180 kHz, which was due to magnetic relaxation. With increasing the field frequency, the coercive force was increased, whereas the magnetization at 50 Oe was decreased. This was because that the magnetization reversal could not follow the change of the applied magnetic field at higher frequency. It was confirmed that magnetization relaxation could be evaluated by these measurements. It has been also shown that areas of hysteresis loops quantitatively agreed with the temperature rise [9], [12].

The efficiency of the self-heating property was estimated using the results of the above-mentioned two measurements. If the heat efficiency calculated from the area of the ac hysteresis measurement is in accordance with that from the self-heating temperature rise, the heat dissipation is attributed to magnetic relaxation losses.

To clarify the contribution of the Néel and Brownian relaxations to the heat dissipation, the ac magnetic susceptibility was measured using a lock-in-amplifier. This measurement was performed for an ac magnetic field of 10 Oe with frequency in the range of 1–1000 kHz. The imaginary component of the ac magnetic susceptibility (χ'') was measured as a function of the frequency [13], [14].

IV. Results and Discussion

A. Heat Dissipation

The self-heating temperature rise of the magnetic iron oxide samples dispersed in water and measured under an ac magnetic field of 50 Oe at 50–500 kHz is plotted in Fig. 4. This figure shows only the results at 500 kHz. The mass of the magnetic iron oxide m_p and the solution m_w were 75 mg and 1500 mg, respectively. The specific heats of the magnetic iron oxide c_p and the solution c_w are 0.92 J/gK and 4.18 J/gK, respectively. The SAR was calculated using the specific heat of the sample, 1.0 J/K and the results of the temperature rise, as indicated by (6). The maximum increase in the temperature was observed for the 86 nm sample.

It is well known that the value of SAR is obtained as the product of the exciting frequency and the efficiency of the heat value. Therefore, the efficiency was calculated by dividing SAR by the frequency, and these results are plotted in Fig. 5. The value of SAR divided by the frequency continued to increase with frequency, and maximum efficiency was not observed within the measured frequency range.

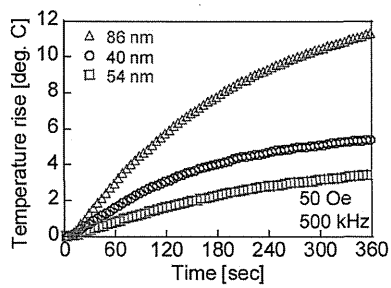

Fig. 4. Self-heating temperature rise of the magnetic iron oxide samples dispersed in water measured under an ac magnetic field of 50 Oe at 500 kHz.

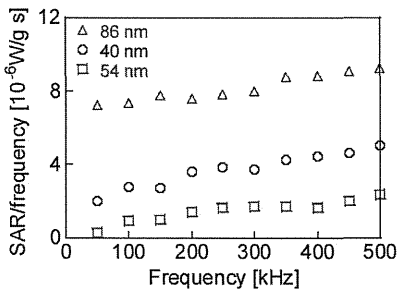

Fig. 5. Specific absorption rate (SAR) of the magnetic iron oxide samples divided by the frequency, which is equivalent to the heat value per cycle of an ac magnetic field.

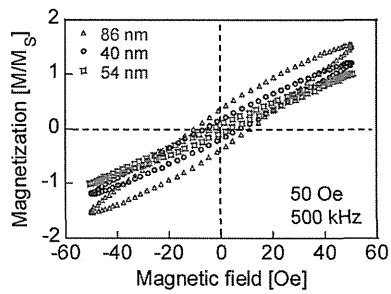

Fig. 6. AC minor hysteresis loops of magnetic iron oxide samples dispersed in water measured under an ac magnetic field of 50 Oe at 500 kHz. The magnetization is normalized by the saturation magnetization (M_s).

B. AC Hysteresis Curves

Fig. 6 shows the ac minor hysteresis curves for the three samples at 500 kHz. All three samples have differently-shaped hysteresis curves. In addition, the shape of the ac hysteresis curves varied according to the frequency, and the area of the curves increased with frequency. This result agrees with the measurement of SAR divided by the frequency (Fig. 7). The dependence of the heat value on the frequency is believed to be due to magnetic relaxation loss. The magnetic relaxation loss per cycle has a maximum value at a certain characteristic frequency. The frequency f_c is calculated by the following equation:

$$f_c = \frac{1}{2\pi\tau} \tag{7}$$

From the hydrodynamic diameters (40, 54, and 86 nm), the f_c for Brownian relaxation was calculated to be 7.59, 2.93, and 0.74 kHz, respectively, using (1), (2), and (7). On the other hand, the f_c for Néel relaxation at 3.6 MHz was also calculated for a primary particle size of 10 nm, and the frequency range of the measurement was higher than f_c for Brownian relaxation. The

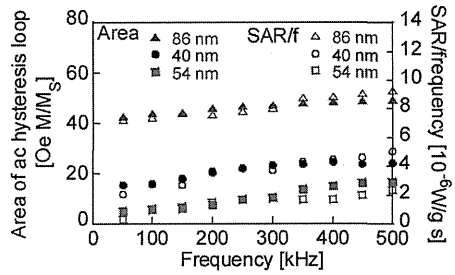

Fig. 7. Comparison of the SAR divided by the frequency with the area of the ac hysteresis loop measured under an ac magnetic field of 50 Oe at 50–500 kHz.

TABLE II
CHARACTERISTIC FREQUENCIES CALCULATED USING THE PRIMARY AND HYDRODYNAMIC DIAMETERS, INCLUDING THE RELAXATION TIMES FOR BROWNIAN RELAXATION τ_B AND NÉEL RELAXATION τ_N, AND THE CHARACTERISTIC FREQUENCIES FOR BROWNIAN RELAXATION f_B AND NÉEL RELAXATION f_N. THE VALUES OF τ_B AND τ_N WERE ESTIMATED USING (1), WHILE THE VALUES OF f_B AND f_N WERE ESTIMATED USING (7)

Hydrodynamic diameter $2r_h$ [nm]	τ_B [μs]	f_B [kHz]	τ_N [ns]	f_N [MHz]
40	21.6	7.36	44.4	3.58
54	54.4	2.93	44.4	3.58
86	216	0.74	44.4	3.58

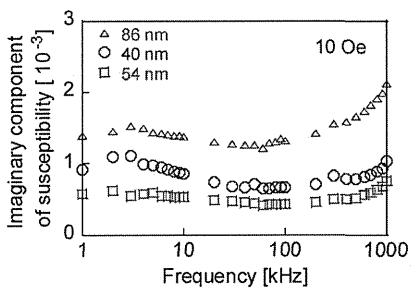

Fig. 8. Imaginary component of the magnetic susceptibility of the magnetic iron oxide samples measured under an ac magnetic field of 10 Oe at 1–1000 kHz.

calculated f_c values for the Brownian and Néel relaxations are summarized in Table II. Therefore, to elucidate the contribution of Brownian relaxation to the heat dissipation, the ac magnetic susceptibility was measured.

C. Magnetic Susceptibility

Fig. 8 shows the imaginary component of the magnetic susceptibility of the samples. The sample with a diameter of 86 nm exhibited a higher value than the samples with diameters of 40 and 54 nm. However, for all of the samples, a peak value of χ'' was not observed at several kHz for the f_c of the Brownian relaxation. Furthermore, the value of χ'' increased with an increase in the frequency up to 1 MHz for the f_c of the Néel relaxation, and the peak value of χ'' would be observed at around 3.6 MHz. Therefore, the dominant mechanism of heat dissipation for these samples is Néel relaxation.

V. CONCLUSION

The self-heating temperature rise, ac hysteresis curve, and magnetic susceptibility of dextran-coated magnetic iron oxide nanoparticles dispersed in water were measured to clarify the contribution of the Néel and Brownian relaxations to heat dissipation. The samples were nanoparticles with different hydrodynamic diameters (40, 54, and 86 nm), but the same primary diameter of 10 nm. SAR divided by the frequency for all three samples increased with frequency. This result agreed with the measured area of the ac hysteresis curves, which were normalized by their saturated magnetization. Furthermore, f_B, which is the peak frequency of the Brownian relaxation, was not observed at several frequencies for the three samples based on evaluation of the imaginary component of the magnetic susceptibility measurements. Therefore, Néel relaxation, which is determined by the primary particle size, was dominant in all three samples. The self-heating temperature rise of the sample with a diameter of 86 nm was higher than that of the samples with diameters of 40 and 54 nm. This result also agreed with the measurement of the ac hysteresis curves. The area of the hysteresis curve was larger, and the value of the maximum magnetization was higher for the 86 nm diameter sample compared to those of the other samples. In addition, the 86 nm diameter sample exhibited a higher value in the imaginary component of susceptibility than that of the other samples, indicating a similar tendency as a function of increasing frequency. These results were due to the difference in the hydrodynamic diameters. Therefore, it was determined that the effect of the magnetic interaction between superparamagnetic nanoparticles depends on the hydrodynamic diameter although the dominant relaxation occurs via Néel relaxation.

REFERENCES

[1] Q. A. Pankhurst, J. Connolly, S. K. Jones, and J. Dobson, "Applications of magnetic nanoparticles in biomedicine," *J. Phys. D. Appl Phys.*, vol. 36, pp. R167–R181, 2003.
[2] A. H. Lu, E. L. Salabas, and F. Schuth, "Magnetic nanoparticles: Synthesis, protection, functionalization, and application," *Angewadte Chemie-International Edition*, vol. 46, pp. 1222–1244, 2007.
[3] T. L. Kline, Y. H. Xu, Y. J. , and J. P. Wang, "Biocompatible high-moment FeCo-Au magnetic nanoparticles for magnetic hyperthermia treatment optimization," *J. Magn. Magn. Mater.*, vol. 321, pp. 1525–1528, 2009.
[4] S. Maenosono and S. Saita, "Theoretical Assessment of FePt nanoparticles as heating elements for magnetic hyperthermia," *IEEE Trans. Magn.*, vol. 42, pp. 2161–2175, 2006.
[5] M. Suto, Y. Hirota, H. Mamiya, A. Fujita, R. Kasuya, K. Tohji, and B. Jeyadevan, "Heat dissipation mechanism of magnetite nanoparticles in magnetic fluid hyperthermia," *J. Magn. Magn. Mater.*, vol. 321, pp. 1493–1496, 2009.
[6] R. E. Rosensweig, "Heating magnetic fluid with alternating magnetic field," *J. Magn. Magn. Mater.*, vol. 252, pp. 370–374, 2002.
[7] I. Hrianca, C. Caizer, and Z. Schlett, "Dynamic magnetic behavior of Fe_3O_4 colloidal nanoparticles," *J. Appl. Phys.*, vol. 92, pp. 2125–2132, 2002.
[8] A. K. Giri, K. M. Chowdary, and S. A. Majetich, "AC magnetic properties of compacted FeCo nanocomposites," *Mater. Phys. Mech.*, vol. 1, pp. 1–10, 2000.
[9] H. Kobayashi, K. Ueda, A. Tomitaka, T. Yamada, and Y. Takemura, "Self-heating property of magnetite nanoparticles dispersed in solution," *IEEE Trans. Magn.*, vol. 47, pp. 4151–4154, 2011.
[10] M. Ma, Y. Wu, J. Zhou, Y. Sun, Y. Zhang, and N. Gu, "Size dependence of specific power absorption of Fe_3O_4 particles in AC magnetic field," *J. Magn. Magn. Mater.*, vol. 268, pp. 33–39, 2004.
[11] M. Kallumadil, M. Tada, T. Nakagawa, M. Abe, P. Southern, and Q. A. Pankhurst, "Suitability of commercial colloids for magnetic hyperthermia," *J. Magn. Magn. Mater.*, vol. 321, pp. 1509–1513, 2009.
[12] B. Mehdaoui, J. Carrey, M. Stadler, A. Comejo, C. Nayral, F. Delpech, B. Chaudret, and M. Respaud, "Influence of a transverse static magnetic field on the magnetic hyperthermia properties and high-frequency hysteresis loops of ferromagnetic FeCo nanoparticles," *Appl. Phys. Lett.*, vol. 100, p. 052403, 2012.
[13] J. Zhang, C. Boyd, and W. Luo, "Two mechanisms and a scaling relation for dynamics in ferrofluids," *Phys. Rev. Lett.*, vol. 77, pp. 390–393, 1996.
[14] O. E. Ayala-Valenzuela, J. A. Matutes-Aquino, J. T. Elizalde Galindo, and C. E. Botez, "Ac susceptibility study of a magnetite magnetic fluid," *J. Appl. Phys.*, vol. 105, p. 07B524, 2009.

frontiers in
INTEGRATIVE NEUROSCIENCE

ORIGINAL RESEARCH ARTICLE
published: 11 November 2013
doi:10.3389/fnint.2013.00076

In vivo evaluation of cellular activity in αCaMKII heterozygous knockout mice using manganese-enhanced magnetic resonance imaging (MEMRI)

Satoko Hattori[1,2,3], Hideo Hagihara[2,3], Koji Ohira[2,3], Ichio Aoki[4], Tsuneo Saga[4], Tetsuya Suhara[1], Makoto Higuchi[1]* and Tsuyoshi Miyakawa[2,3,5]*

[1] *Molecular Neuroimaging Program, Molecular Imaging Center, National Institute of Radiological Sciences, Chiba, Japan*
[2] *Division of Systems Medical Science, Institute for Comprehensive Medical Science, Fujita Health University, Toyoake, Aichi, Japan*
[3] *Japan Science and Technology Agency (JST), Core Research for Evolutional Science and Technology (CREST), Kawaguchi, Saitama, Japan*
[4] *Diagnostic Imaging Program, Molecular Imaging Center, National Institute of Radiological Sciences, Chiba, Japan*
[5] *Center for Genetic Analysis of Behavior, National Institute for Physiological Sciences, Okazaki, Aichi, Japan*

Edited by:
John J. Foxe, Albert Einstein College of Medicine, USA

Reviewed by:
Sebastian Cerdan, Instituto de Investigaciones Biomedicas Alberto Sols, Spain
Hadley Creighton Bergstrom, National Institutes of Health, USA

***Correspondence:**
Tsuyoshi Miyakawa, Division of Systems Medical Science, Institute for Comprehensive Medical Science, Fujita Health University, 1-98 Dengakugakubo Kutsukake-cho, Toyoake, Aichi 470-1192, Japan
e-mail: miyakawa@fujita-hu.ac.jp
Makoto Higuchi, Molecular Neuroimaging Program, Molecular Imaging Center, National Institute of Radiological Sciences, 4-9-1, Anagawa, Inage-ku, Chiba 263-8555, Japan
e-mail: mhiguchi@nirs.go.jp

The alpha-calcium/calmodulin-dependent protein kinase II (αCaMKII) is a serine/threonine protein kinase predominantly expressed in the forebrain, especially in the postsynaptic density, and plays a key role in synaptic plasticity, learning and memory. αCaMKII heterozygous knockout (HKO) mice exhibit abnormal emotional and aggressive behaviors and cognitive impairments and have been proposed as an animal model of psychiatric illness. Our previous studies have shown that the expression of immediate early genes (IEGs) after exposure to electric foot shock or after performing a working memory task is decreased in the hippocampus, central amygdala, and medial prefrontal cortex of mutant mice. These changes could be caused by disturbances in neuronal signal transduction; however, it is still unclear whether neuronal activity is reduced in these regions. In this study, we performed *in vivo* manganese-enhanced magnetic resonance imaging (MEMRI) to assess the regional cellular activity in the brains of αCaMKII HKO mice. The signal intensity of MEMRI 24 h after systemic $MnCl_2$ administration reflects functional increases of Mn^{2+} influx into neurons and glia via transport mechanisms, such as voltage-gated and/or ligand-gated Ca^{2+} channels. αCaMKII HKO mice demonstrated a low signal intensity of MEMRI in the dentate gyrus (DG), in which almost all neurons were at immature status at the molecular, morphological, and electrophysiological levels. In contrast, analysis of the signal intensity in these mutant mice revealed increased activity in the CA1 area of the hippocampus, a region crucial for cognitive function. The signal intensity was also increased in the bed nucleus of the stria terminalis (BNST), which is involved in anxiety. These changes in the mutant mice may be responsible for the observed dysregulated behaviors, such as cognitive deficit and abnormal anxiety-like behavior, which are similar to symptoms seen in human psychiatric disorders.

Keywords: αCaMKII, manganese-enhanced MRI, immature, dentate gyrus, hippocampus, bed nucleus of stria terminalis, schizophrenia, psychiatric disorder

INTRODUCTION

The alpha isoform of calcium/calmodulin-dependent protein kinase II (αCaMKII) is a calcium-activated, serine/threonine protein kinase and is abundant in the brain. It is enriched at the postsynaptic density (Lisman et al., 2002), and its activity is necessary for long-term potentiation of synaptic transmission in the hippocampus that may regulate learning and memory. Previous studies have shown that spatial learning and memory are affected in both homozygous and heterozygous αCaMKII knockout mice (Silva et al., 1992, 1996; Gordon et al., 1996; Frankland et al., 2001; Elgersma et al., 2002), as well as in several strains of αCaMKII transgenic mice (reviewed in Elgersma et al., 2004).

αCaMKII heterozygous knockout (HKO) mice also have various behavioral abnormalities that resemble symptoms seen in human psychiatric disorders, including decreased fear response, enhanced defensive aggression (Chen et al., 1994), increased locomotor activity, deficit in working memory, high level of social aggression toward cage mates, and an exaggerated infradian rhythm (Yamasaki et al., 2008). We found that molecular, morphological, and electrophysiological features in the dentate gyrus (DG) neurons of adult mutant mice were similar to those of immature DG neurons in normal rodents (Yamasaki et al., 2008). The "immature dentate gyrus (iDG)" phenotype has been observed in the post-mortem brains of patients with schizophrenia and bipolar disorder (Walton et al., 2012), as well as in other

mouse models of these disorders (Hagihara et al., 2011; Ohira et al., 2013; Takao et al., 2013). In addition, levels of dopamine D2 receptors in a state with a high affinity for dopamine ($D2^{High}$ receptors) were found to be elevated in the striatum of αCaMKII HKO mice, which could be representative of the hyperdopaminergic state seen in patients with schizophrenia (Novak and Seeman, 2010). Therefore, it has been proposed that αCaMKII HKO mice are promising animal models of schizophrenia and other psychiatric disorders (Yamasaki et al., 2008; Novak and Seeman, 2010) and that the iDG might serve as a novel endophenotype of the disorders, (Walton et al., 2012; Hagihara et al., 2013).

Our previous studies have shown that αCaMKII HKO mice had marked abnormalities in neurotransmitter binding to their receptors and neuronal activity in several brain regions (Yamasaki et al., 2008; Matsuo et al., 2009). Quantification of the expression of immediate-early genes (IEGs), which are activated in response to neuronal stimuli, exhibited lower expression levels of c-Fos in the DG, CA3, and central amygdaloid nucleus of the mutant mice than those of the wild-type mice following electric foot shock (Yamasaki et al., 2008). In the αCaMKII HKO mice, following a working memory version of the eight-arm radial maze task, the expressions of c-Fos were reduced in neurons of the hippocampal DG, CA1, and CA3 areas, central amygdala, and medial prefrontal cortex, whereas their expressions in the mutant mice kept in home cages were decreased in the DG, but not in other areas (Matsuo et al., 2009). In addition, the neurons in the mutant DG had abnormal electrophysiological features, including high excitability, small spike amplitude, and a decreased number of spikes during sustained depolarization (Yamasaki et al., 2008). These results suggest that αCaMKII HKO mice have functional deficits in several brain regions. However, it is possible that the altered expression of such IEGs is caused by a disruption in the signaling pathways that link neuronal activity to transcription, and it remains unclear whether neuronal activity is also altered in these regions of the mutant mice.

In this study, we evaluated the brains of αCaMKII HKO mice using systemically Mn^{2+} administrated MEMRI without blood-brain-barrier disruption (Watanabe et al., 2001; Aoki et al., 2004). This is an effective method to detect and visualize the anatomical and functional features of the brain. Mn^{2+} is a positive contrast agent for MRI and can accumulate in excitable cells via some of the transport mechanisms shared with calcium, such as voltage-gated Ca^{2+} channels and ionotropic glutamate receptors (Itoh et al., 2008; Silva and Bock, 2008; Hankir et al., 2012). The signal intensity on a T_1-weighted (T_1W) MR image is enhanced by Mn^{2+} uptake through activated ion channels; therefore, this technique can reflect the cellular activity in brain regions (Yu et al., 2005). We performed MRI scans on αCaMKII HKO and wild-type mice 1 day after systemic $MnCl_2$ intravenous administration, and assessed the normalized signal intensity under baseline conditions in the home cage.

MATERIALS AND METHODS

ANIMALS AND EXPERIMENTAL DESIGN

αCaMKII HKO mice generated by gene-targeting techniques were obtained from Jackson Laboratories (Bar Harbor, ME, USA). Mice were housed one per cage in a room with a 12 h light dark cycle (light on at 7:00 a.m.) with access to food and water *ad libitum*. MEMRI was performed on 7 to 10 month-old αCaMKII HKO mice ($n = 7$) and wild-type littermates ($n = 7$) on a C57BL/6J background. The Institutional Animal Care and Use Committee of the National Institute of Radiological Sciences and Fujita Health University approved the present experimental protocol.

MANGANESE ADMINISTRATION

Prior to the administration, 100 mM of $MnCl_2$ ($MnCl_2$-$4H_2O$, Sigma-Aldrich, St. Louis, MO, USA) was made with distilled water and diluted to 50 mM with saline to match the osmotic pressure of blood. We slowly infused 75 mg/kg (380 μmol/kg) $MnCl_2$ (total volume: 0.2–0.3 mL) for 60 min through the tail vein using a syringe pump (KDS-100, KD Scientific, Holliston, MA, USA). The $MnCl_2$ dose used in this study provided clear regional contrast and was similar to the doses used in previous MEMRI studies of the mouse brain (Yu et al., 2005; Lutkenhoff et al., 2012; Perez et al., 2013). After $MnCl_2$ injection, each mouse showed reduced locomotor activity temporarily for approximately 2–3 h, probably due to the toxic effect of $MnCl_2$. We did not notice any apparent differences in the behavioral response to $MnCl_2$ between genotypes. Mice were kept anesthetized with 0.5–1.5% isoflurane (Mylan Inc., Tokyo, Japan) during $MnCl_2$ infusion. Rectal temperature was continuously monitored and automatically maintained at approximately 37.5°C using a temperature controller (E5GN, Omron, Inc., Kyoto, Japan) and electrical heating pad (SG-15, Showa-Seiki industry, Inc., Kobe, Japan).

ANIMAL PREPARATION AND MRI MEASUREMENTS

We performed MRI in a 7.0 Tesla scanner, with a 40 cm bore magnet (Kobelco and Jastec, Tokyo, Japan) interfaced with a Bruker Avance-I console (BioSpec, Bruker Biospin, Ettlingen, Germany) with a volume coil for transmission (Bruker Biospin, Ettlingen, Germany) and a two-channel phased-array coil for reception (Rapid Biomedical, Rympar, Germany). Mice were anesthetized with 1.0–2.0% isoflurane and placed in prone position. During the experiment, a warm airflow over the animal was used to maintain its rectal temperature at 37.5°C. Respiratory rate was maintained at 20–40 breaths per minute and monitored throughout the experiment. Two-dimensional single-slice T_1W images were obtained by conventional spin-echo sequence with the following parameters: pulse repetition time (TR) = 250 ms; echo time (TE) = 9.574 ms; matrix size = 192 × 192; field of view = 1.92 × 1.92 cm^2; slice thickness = 1.0 mm; slice gap = 1 mm; spatial resolution = 100 × 100 × 1000 μm^3; and number of acquisitions = 4. A complete set of T_1W measurements consisted of two T_1W scans with slice offsets of 0 and 1 mm to maintain continuity of slices and to cover the entire brain. To register the image plane exactly, anatomical scout images were acquired using an incoherent, gradient-echo, fast low-angle shot sequence (TR = 100 ms; TE = 6 ms; matrix = 256 × 256; slice thickness = 2.0 mm). The slice orientation of the coronal plane was carefully adjusted on the sagittal scout image according to the landmarks of the pituitary body with reference to a mouse brain atlas (Paxinos and Franklin, 2001).

MRI DATA ANALYSIS

MR image data were converted from native Bruker format to voistat and TIFF files using PMOD (version 2.6; PMOD Technologies, Zurich, Switzerland), and analyzed quantitatively with PMOD and ImageJ.[1] Through comparison of MR images with a mouse brain atlas (Paxinos and Franklin, 2001), regions of interest (ROIs) for quantitative analysis of MEMRI were defined and delineated manually in the hippocampus, bed nucleus of the stria terminalis (BNST), cortex, striatum, thalamus, midbrain, and amygdala. We compared the MR image with the atlas based on the distance from the pituitary. Signal intensity was measured in each ROI, and we present the data normalized to that in the whole brain (Perez et al., 2013). In many cases, a slight signal intensity gradient was observed that could change within a plane and serve as noise. To minimize such noise, we used the average signal intensity of whole brain for normalization.

Statistical analyses were conducted using StatView software (SAS Institute, Cary, NC, USA). All data are presented as the mean ± the standard error of the mean (SEM), and were analyzed by one-way analysis of variance (ANOVA). An alpha level adjusted for multiple comparisons was calculated for each brain region by Bonferroni-Holm method.

QUANTIFICATION OF CELL NUMBER

Adult αCaMKII HKO mice ($n = 3$) and wild-type littermates ($n = 3$) were used. They were perfused through the heart with ice-cold phosphate buffered saline (PBS) and then with 4% paraformaldehyde (PFA) in 0.1 M PBS, with pH 7.4. After perfusion, the brains were immediately removed and immersed in the same fixative at 4°C overnight, followed by successive immersions in 30% sucrose in PBS. The brains were mounted in Tissue-Tek (Miles Inc., Elkhart, NY, USA), frozen, and stored at −80°C until use. Brains were sliced coronally into 10 μm thick sections on a cryostat (CM1850, Leica Microsystems, Wetzlar, Germany). The sections were stained with Hoechst 33258 (Polyscience, Warrington, PA, USA). Fluorescent signals were detected using a confocal laser-scanning microscope (LSM 700, Zeiss, Oberkochen, Germany). For the quantification of region size and Hoechst-stained cell numbers, we used ImageJ with the WCIF ImageJ bundle[2] (Takao et al., 2013). Three sections obtained from the anterior hippocampal region (from bregma −1.70 mm to bregma −2.30 mm, approximately) per animal were examined. ROI were delineated manually on the Hoechst-stained images with reference to the mouse brain atlas (Paxinos and Franklin, 2001). The values were then averaged within each brain and by group. All data collected in quantitative analyses were statistically evaluated using Student's *t*-test for comparison of means.

RESULTS

Normalized signal intensities of MEMRI responses in several anatomically defined ROIs were calculated semiquantitatively in αCaMKII HKO and wild-type mice. **Figure 1A** shows T_1W MR images of horizontal and coronal slices 1 day after $MnCl_2$ administration. The normalized signal intensity in MEMR images was significantly lower in the DG of mutant mice than in the DG of wild-type mice (**Figures 1A, B**, mutant vs. wild-type: 1.317 ± 0.007 vs. 1.397 ± 0.012, $F_{1,12} = 46.994$, $p < 0.0001$; adjusted $\alpha = 0.0063$). In contrast, the CA1 field including stratum radiatum, which is a projection area of the CA3, showed higher signal enhancement in αCaMKII HKO mice (**Figure 1A**). Normalized signal intensity was significantly higher in the CA1 of mutant mice than in the CA1 of wild-type mice (**Figure 1B**, mutant vs. wild-type: 1.215 ± 0.005 vs. 1.165 ± 0.005, $F_{1,12} = 71.086$, $p < 0.0001$; adjusted $\alpha = 0.0056$). However, there was no significant difference in normalized signal intensity in the CA3 region between the two genotypes (**Figure 1B**, mutant vs. wild-type: 0.937 ± 0.008 vs. 0.934 ± 0.016, $F_{1,12} = 0.041$, $p = 0.8438$). A scatter plot showing the relationship between normalized signal intensity in the DG and CA1 field (**Figure 1C**) indicates that the subregional profile of hippocampal cellular activity in the αCaMKII HKO mice is clearly distinct from that in the normal mice.

Signal intensity in MEMRI could reflect cell density in addition to cellular activity. The cell density in the mutant mice was assessed by Hoechst stain. In the DG, a significant increase in cell density was detected in the mutant mice (mutant vs. wild-type: 2357 ± 83 vs. 1578 ± 57, $p = 0.0012$) as compared to in the wild-type mice, which is likely the result of greatly increased adult neurogenesis in the DG of mutant mice (Yamasaki et al., 2008). There were no significant differences in cell density in the CA1 (mutant vs. wild-type: 1256 ± 8 vs. 1234 ± 45, $p = 0.2026$) and CA3 fields (mutant vs. wild-type: 552 ± 6 vs. 581 ± 18, $p = 0.4926$) between genotypes. In general, signal intensity in MEMRI is expected to be positively correlated with cell density (Silva et al., 2004), given that there is no difference in cellular activity. However, in the mutant mice, the signal intensity of the DG decreased, while cell density increased. These results suggest that decreased signal intensities in mutant mice are due to decreased cellular activity, not to increased cell density. Total cell numbers counted were 112.3 ± 11.9 in wild-type mice and 159.3 ± 2.9 in mutant mice in the dorsal part of the granule cell layer ($p = 0.0183$), 87.7 ± 7.5 in wild-type mice and 88.7 ± 3.2 in mutant mice in the pyramidal cell layer of CA1 ($p = 0.9084$), and 130.7 ± 7.5 in wild-type mice and 154.7 ± 6.6 in mutant mice in the pyramidal cell layer of CA3 ($p = 0.0742$).

In addition to the hippocampus, we observed increased MEMRI signal in the BNST of αCaMKII HKO mice (**Figure 2A**), and normalized signal intensity of the BNST was significantly higher in mutant mice than in wild-type mice (**Figure 2B**, mutant vs. wild-type: 1.024 ± 0.009 vs. 0.983 ± 0.012, $p = 0.0069$; adjusted $\alpha = 0.0071$). We also estimated normalized signal intensity in the major regions of the brain, such as the cortex, striatum, thalamus, midbrain, and amygdala. No significant differences were observed in the signal intensity of MEMRI in these regions between genotypes (**Figure 2C**, cortex: $F_{1,12} = 0.174$, $p = 0.6836$; striatum: $F_{1,12} = 0.090$, $p = 0.7691$; thalamus: $F_{1,12} = 0.005$, $p = 0.9442$; midbrain: $F_{1,12} = 1.390$, $p = 0.2613$; amygdala: $F_{1,12} = 0.127$, $p = 0.7273$). We also analyzed the data using signal intensities of the cortex or striatum for normalization, which yielded essentially the same results as those derived from the analysis using the signal intensities of the whole brain for normalization (data not shown).

[1] http://rsb.info.nih.gov/ij/download.html

[2] http://www.uhnresearch.ca/facilities/wcif/download.php

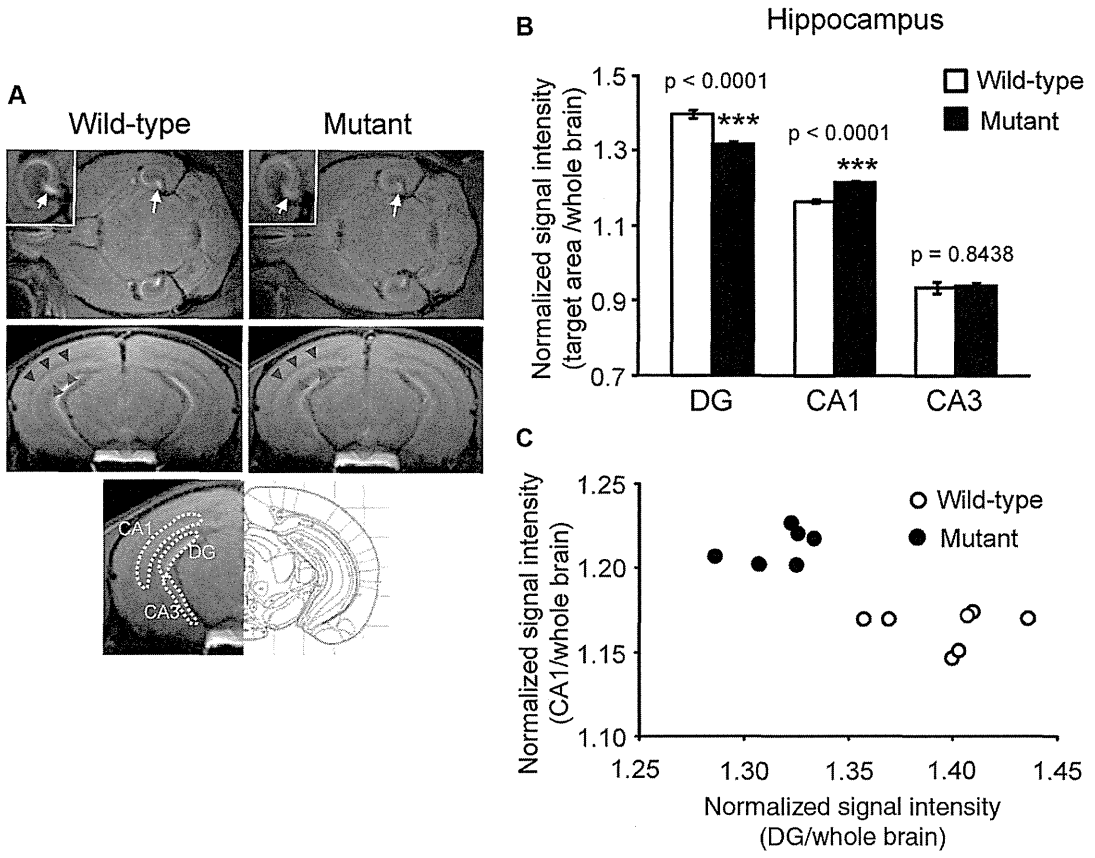

FIGURE 1 | Signal intensity decreased in the DG and increased in the CA1 region of αCaMKII HKO mice. (A) Representative T_1W MR images after systemic $MnCl_2$ administration. The top row shows horizontal slices at the level of the hippocampus. White squares indicate areas of the hippocampus presented at a high magnification. White arrows indicate the V-shaped structure of the DG. The middle row shows coronal slices including the hippocampal structure (bregma: −3.08 mm). The CA1 and stratum radiatum, including the projection area of the CA3, are indicated by red and blue arrowheads, respectively. The bottom row shows the anatomical location of ROIs in the hippocampus. The ROIs correspond to the DG, CA1, and CA3, respectively. **(B)** Normalized signal intensities in the hippocampal subregions are presented as the mean ± SEM. The *p* values indicate genotype effect in one-way ANOVA. **(C)** Scatterplot of normalized signal intensity in the DG versus CA1 region.

DISCUSSION

The αCaMKII HKO mouse has been proposed as an animal model of psychiatric illnesses, including schizophrenia and bipolar disorders. In this study, MEMRI demonstrated that Mn^{2+} accumulation was reduced in the DG and elevated in the BNST and CA1 field of the hippocampus.

We previously reported that αCaMKII HKO mice exhibited the iDG phenotype, a potential brain endophenotype shared by patients with schizophrenia and bipolar disorder (Walton et al., 2012; Hagihara et al., 2013; Shin et al., 2013). In the mutant DG, IEGs expression is abolished almost completely following a working memory task and electric foot shocks (Yamasaki et al., 2008; Matsuo et al., 2009), and electrophysiological evidence has revealed a decrease in the number of spikes during sustained depolarization (Yamasaki et al., 2008). These findings suggest that there is a decrease in neuronal activity and/or a disruption in the signal transduction pathway required to induce IEGs in the mutant DG. In this study, we examined the activity profile in the brains of mutant mice by performing MEMRI. A lower signal intensity of MEMRI was observed in the V-shaped structure of the DG in αCaMKII HKO mice than in that of the wild-type mice, and this might be the result of reduced activity in DG granule cells. Several lines of evidence support the reduction of activity in the DG. Downregulation in the expression levels of Ca^{2+}-permeable receptors could lead to the low activity observed in the DG of mutant mice. We have reported a decrease in N-methyl-D-aspartate (NMDA) receptor binding by using autoradiographic techniques (Yamasaki et al., 2008). Decreased Mn^{2+} influx through these receptors could be detected on the MEMRI as differences in Mn^{2+}-enhanced signal intensity in the granule cells of mutant mice. Alternatively, the activation of local circuits by immature neurons in the DG could inhibit the activity of the entire DG. Lacefield et al. proposed the possibility that immature granule cells effectively drive hilar interneurons, which innervate back to all granule cells (Lacefield et al., 2012). Thus, an excess of immature neurons may cause gross inhibition of the DG by

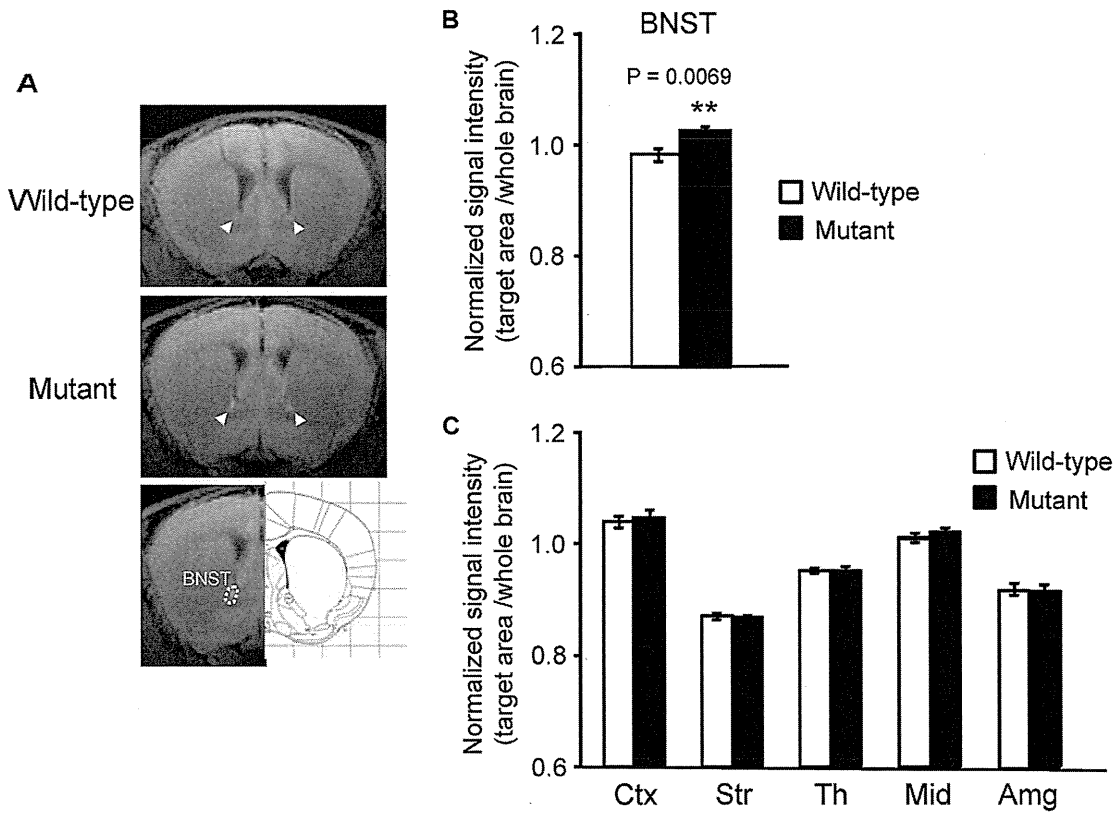

FIGURE 2 | Signal intensity increased in the BNST of αCaMKII HKO mice. **(A)** Representative T_1W MR images after systemic $MnCl_2$ administration. The top and middle rows show coronal slices at the level of the BNST (bregma: + 0.62 mm). The BNST is indicated by white arrowheads. The bottom row shows the anatomical location of ROIs in the BNST. **(B)** Normalized signal intensity in the BNST is presented as the mean ± SEM for the indicated numbers of animals **(C)** Normalized signal intensities in other regions of the brain are presented as the mean ± SEM.The *p* values indicate the effect of genotype in one-way ANOVA.

a feedback loop and result in the reduced enhancement of MRI signal intensity observed in the DG of mutant mice.

In contrast to the DG, the CA1 field of the αCaMKII HKO mice showed greater Mn^{2+} uptake, especially the stratum radiatum, which contains projection fibers to CA1 neurons. This result supports the idea of increased activity in the CA1 field of mutant mice. One possibility is that the augmentation in CA1 neuronal activity could be caused by an altered response to inputs from the entorhinal cortex (EC). The hippocampus mainly includes two excitatory networks, the monosynaptic pathway (from layer III in EC to CA1) and the trisynaptic pathway (from layer II in EC to DG to CA3 to CA1) (Amaral and Witter, 1989). Dysfunction in the mutant DG could reduce neuronal transmission in the trisynaptic pathway, and, therefore, homeostatic regulation of hippocampal network activity might lead to an increase in monosynaptic excitation of the CA1 region. Additionally, the decreased activity in the DG of these mice might cause activation in the CA3 and then in the CA1 field. Mossy fibers from the DG release the excitatory neurotransmitter glutamate (Henze et al., 2000). In the CA3, mossy fibers project to GABAergic interneurons that provide inhibitory inputs to CA3 pyramidal cells, and also terminate in CA3 pyramidal neurons (Henze et al., 2000). Activity of the DG and mossy fibers may result in a net inhibition within the CA3 network and presumably activate only a specific subset of CA3 pyramidal neurons (Henze et al., 2000; Song et al., 2012). In the αCaMKII HKO mice, decreased DG activity may lead to a tonic net activation of the CA3 and CA1 through a trisynaptic pathway. In this study, no difference in the MEMRI signal intensity ratio between genotypes could be detected in the CA3 area. This might result from limitations related to our methodology, including spatial resolution and detection sensitivity. Finally, the increased activity might be an effect of the HKO of αCaMKII itself in cells present in the CA1 area. Our previous study demonstrated a downregulation in serotonin 1A receptor binding and an upregulation of serotonin transporter binding in the CA1 of mutant mice (Yamasaki et al., 2008). Such abnormalities in the CA1 may have caused the increased activity. Further detailed studies, combined with *in vivo* imaging and electrophysiological methods, are needed to address the activity in each hippocampal subregion of the mutant mice.

A previous study revealed that the area showing enhanced signal on Mn^{2+}-contrasted MRI corresponds to the area that

exhibits increased expression of IEGs (Morita et al., 2002). In the DG, our result is consistent with this observation. However, there is a discrepancy between MEMRI signal intensity and c-Fos expression in the CA1. The expression of c-Fos following a working memory task was decreased in the mutant (Matsuo et al., 2009), and there was no significant difference in its expression in the CA1 of both genotypes after electrical foot shock and when the mice were kept in the home cage (Yamasaki et al., 2008; Matsuo et al., 2009). The inconsistency may be due to signal transduction abnormalities in IEG expression and/or to differences in experimental conditions, including the type of stimuli presented to the mice.

Additionally, previous studies suggested that the accumulation of reactive astrocytes and/or the migration of microglia could also cause increased signal intensity of MEMRI (Widerøe et al., 2009; Kawai et al., 2010). In αCaMKII HKO mice, the expression of glial fibrillary acidic protein, a well-established marker of astrocytes, is increased in the DG and CA1 area, especially the stratum radiatum and stratum oriens (unpublished data). In contrast, no significant difference between genotypes was observed in the immunoreactivity of ionized calcium binding adaptor molecule 1, a microglia/macrophage-specific calcium binding protein, in either the DG or CA1 field (unpublished data). These data suggest that decreased Mn^{2+} uptake in the mutant DG could be mainly due to altered neuronal activity. On the other hand, it is possible that the increased signal intensity of MEMRI, which was observed in the CA1 of mutant mice, was influenced by an increase in reactive astrocytes as well as by changes in neuronal activity.

In αCaMKII HKO mice, altered signal intensity in MEMRI was observed in the hippocampus, a region that plays a key role in cognitive functions such as working memory (Goldman-Rakic, 1994) and pattern separation (Gilbert et al., 2001; Gilbert and Kesner, 2003; Lee and Kesner, 2004a,b; Leutgeb et al., 2007; McHugh et al., 2007; Nakashiba et al., 2008). Impairments in hippocampal function are often observed in patients with psychiatric disorders such as schizophrenia and anxiety disorders (Goldman-Rakic, 1994) and may represent a behavioral endophenotype of these disorders. We demonstrated that αCaMKII HKO mice had severe deficits in working memory (Yamasaki et al., 2008), and that the density of c-Fos-positive cells in the hippocampus after a working memory task was significantly lower in the mutant mice than in the wild-type mice (Matsuo et al., 2009). In the EC of mutant mice, IEG expression was induced to the same extent as that observed in wild-type mice after the task. Thus, reduced or aberrant neuronal activity in the DG, which is a key input node for the hippocampal trisynaptic pathway, might lead to altered hippocampal network activity and impaired working memory performance in mutant mice. Indeed, previous studies have shown that rats with lesions of the DG are impaired in their ability to perform a working memory version of the eight-arm radial maze task (McLamb et al., 1988; Emerich and Walsh, 1989; Morris et al., 2012). It is possible that working memory dysfunction in mutant mice is caused by impaired rapid encoding of spatial information.

The mutant mice also showed increased MEMRI signal intensity in the BNST. This region has roles in the regulation of the hypothalamic-pituitary-adrenal axis response to acute stress (Choi et al., 2007). Recent studies in mice demonstrated that the oval nucleus increases anxiety-like behavior, while anterodorsal subregions of the BNST decrease anxiety-like behavior (Kim et al., 2013), and that BNST excitatory and inhibitory projections differentially produce anxiogenic and anxiolytic behavioral phenotypes, respectively (Jennings et al., 2013). These findings suggest that BNST acts as a crucial circuit node for bidirectional regulation of anxiety related responses. It is possible that increased BNST activity underlies decreased anxiety-like behavior in the αCaMKII mutant mice. During a casual visual inspection of the images, we noticed that the signal intensity was obviously increased in a discrete region of the BNST. There is a possibility that we could detect differences in signal intensities in other brain subregions as well. Future studies, using voxel-based analyses, are needed to assess the differences in detail.

In this study, we evaluated *in vivo* cellular activity in the brains of αCaMKII HKO mice by using MEMRI. It has been proposed that these mice are useful animal models of neuropsychiatric disorders (Yamasaki et al., 2008; Novak and Seeman, 2010; Hagihara et al., 2013; Shin et al., 2013). Our study is the first application of *in vivo* MEMRI in the mutant mice that focused on baseline activity rather than stimulus driven activity. Reduced excitatory signaling in the DG and increased activity in the CA1 appear to be associated with the pathological features of schizophrenia (Schobel et al., 2009; Tamminga et al., 2010). The results of the current study also suggest that cellular activity decreases in the DG and increases in the CA1 of mutant mice, providing additional support for the validity of these mice as an animal model of these disorders. The iDG and abnormal behavioral phenotypes are shared with Shn-2 knockout (Takao et al., 2013), mutant SNAP-25 knock-in (Ohira et al., 2013), and forebrain-specific calcineurin knockout mice (unpublished data). Chronic fluoxetine treatment and pilocarpine-induced seizures also lead to the iDG phenotype (Kobayashi et al., 2010; Shin et al., 2013). It is of interest to examine whether these mice show similar patterns of Mn^{2+} accumulation in MEMRI. Moreover, recent studies have demonstrated regional alteration of cellular activity in other animal models of neuropsychiatric disorders (Lutkenhoff et al., 2012; Perez et al., 2013). In addition to these studies, our results suggest that non-invasive MRI measurement is applicable for translational research of neuropsychiatric disorders. MEMRI of mutant mice would also provide biological outcome measures in screening of novel therapeutic compounds targeting these disorders.

ACKNOWLEDGMENTS

We thank Misao Yoneyama, Sayaka Shibata, and Takeo Shimomura for skillful assistance with the MR imaging experiments and Takeharu Minamihisamatsu for the maintenance and preparation of transgenic mice. This work was supported by grants from CREST of Japan Science and Technology Agency (JST), Grants-in-Aid for Japan Advanced Molecular Imaging Program and Scientific Research on Innovative Areas ("Brain Environment") from the Ministry of Education, Culture, Sports, Science and Technology, Japan, and partially by KAKENHI grant from the Japan Society for the Promotion of Science (JSPS).